Monte Carlo simulations for under-water radon measurements

Melchionda Nicola

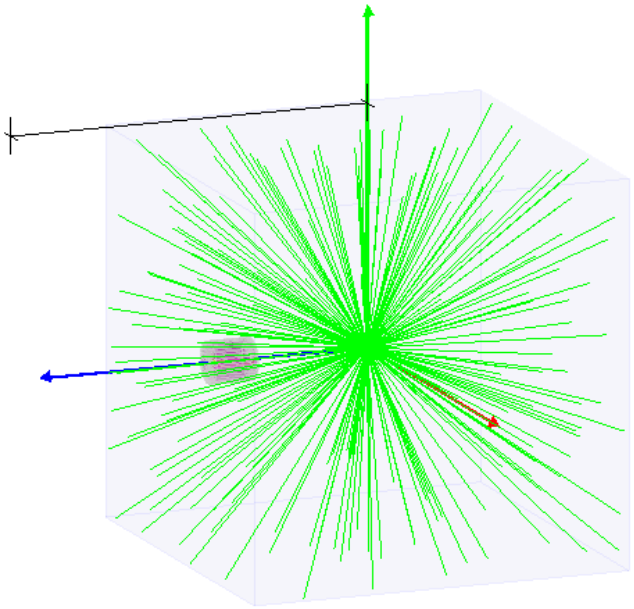

SH204X Degree Project in Physics
Second Cycle 30 credits
SE-100 44 STOCKHOLM

POLITECNICO DI TORINO

MASTER's Degree in Nuclear Engineering

MASTER's Degree Thesis

MONTE CARLO SIMULATIONS FOR UNDER-WATER RADON MEASUREMENTS

Supervisors

Dr. Torbjörn Bäck

Prof. Fabio Subba

Candidate

Nicola Melchionda

March 2025

Sammanfattning

Följande examensarbete har utförts som en del av det europeiska projektet ArtEmis, vars huvudsyfte är att undersöka möjligheten att använda den ökade koncentrationen av den radioaktiva gasen radon som ett förstadium till jordbävningar.

Bland naturkatastroferna är jordbävningar särskilt vanliga och de orsakar tusentals dödsfall varje gång de inträffar med stor magnitud. Den höga dödligheten beror till stor del på att jordbävningar är oförutsägbara, både i tid och rum, även om områden med högre seismisk aktivitet kan identifieras utifrån geologiska studier och statistiska uppgifter. Före en jordbävning bildas mikrosprickor i de omgivande stenstrukturerna på grund av påfrestningar, vilket frigör större mängder radongas än vanligt i bergets porer. Ett sätt att hitta ett förstadium till en jordbävning skulle vara att mäta den gammastrålning som avges efter sönderfallet av radon. Med detta syfte kan man placera strålningsdetektorer i områden med hög seismicitet för att övervaka eventuella förändringar i radonaktivitetsnivåerna. Detta kan göras i jord, grundvatten (via källor, brunnar och borrhål) eller luft. Detta examensarbete syftar till att simulera detekteringen av γ-fotoner som avges av sönderfallet av radon och andra isotoper i en vattenmiljö för att hitta användbara resultat för utvecklingen av projektet.

I denna avhandling kommer det att konstateras att det verkliga gammaspektrumet från den studerade platsen i Italien och det simulerade spektrumet uppvisar liknande egenskaper, vilket är användbart för att utföra många studier av beteendet hos radonsönderfallsprocessen i vatten. Effekterna av kaliumet i väggen undersöks och den kraftiga effekten av vatten som en skärm för strålning framgår tydligt av simuleringarna, även i jämförelse med fallet med en detektor i en luftmiljö. Dessutom kommer det att visas att för att titta på variationerna i radonkoncentrationen är det lämpligt att använda ett bredare spektrum istället för ett mindre runt en topp.

Abstract

The following Master Thesis has been performed as part of the European project ArtEmis, whose main goal is to investigate the possibility of using the increased concentration of the radioactive gas radon as an earthquake precursor.

Among the natural disasters, earthquakes are particularly frequent and cause thousands of deaths whenever they hit with a large magnitude. Their high mortality is mainly due to their unpredictability in space and time, even though areas with a higher seismic activity can be identified based on geological studies and statistical records. Before an earthquake, microcracks are formed in the surrounding stone structures due to stress, releasing greater than usual amounts of radon gas within the rock pores. A way of finding an earthquake precursor would be to measure the gamma-ray radiation emitted after the radon decay. With this aim, one can place radiation detectors in areas with high seismicity in order to monitor possible changes in radon activity levels. This could be done in soil, groundwater (via springs, wells, and boreholes), or air. This Master Thesis aims to simulate the detection of γ photons emitted by the decay of radon and other isotopes inside a water environment to find useful results for the project development.

In this thesis, it will be found that the real gamma spectrum of the studied site in Italy and the simulated one show similar features, which are useful for performing many studies of the behavior of the radon decay process in water. A reasonable volume of water affecting the detected spectrum will be found to acquire a better knowledge of the physics at the studied site and help perform the simulations. The effects of the potassium in the wall are investigated, and the potent effect of water as a screen for radiation is made evident through the simulations, also in comparison with the case of a detector in an air environment. Moreover, it will be shown that looking at the variations in the radon concentration, it is convenient to use a broader spectrum instead of a smaller one around a peak.

FOREWORD

I would like to thank professors Ayse Nyberg and Torbjörn Bäck, from KTH, for introducing and allowing me to participate in the ArtEmis project. Their competent assistance and help in developing this thesis have been very valuable. I also express my gratitude to all the students participating in the ArtEmis project, whose work has been helpful in writing this thesis, in particular Maja Walfridson and the students of the KEX group. Moreover, I am grateful to my referent at Politecnico di Torino, professor Fabio Subba, for his useful feedback and advice.

Nicola Melchionda

Turin, Italy, September 2024

TABLE OF CONTENTS

1 INTRODUCTION

This chapter presents the background, purpose, limitations, and method used in this thesis to give an overview of the work.

1.1 Background

The forecasting of earthquakes is a widely debated topic. Although there is no reliable method to predict an earthquake nowadays, many studies have been performed over time, and some promising results have been identified. The ArtEmis project aims to continue the work that started with those studies and get some valuable results for developing knowledge of radon as an earthquake precursor. This thesis has been written to contribute to understanding the detection of the gamma photons emitted in radon decay and the effects of water as the medium in which the detector is placed. Measuring radon in water is more challenging than in air due to the short mean path of alpha particles in water and the harsh conditions for detector materials. On the other hand, it is essential to minimize the numerous 'false' peaks in radon measurements in air or soil caused by natural variations in environmental factors such as temperature, air pressure, wind, humidity, rainfall, and the sun cycle.

ArtEmis (Awareness and resilience through European multi-sensor system) is a European project whose main aim is to investigate the relationship between seismic activity throughout the continent and the fluctuations in radon concentration over space and time. This will be achieved by installing over 100 sensors along fault zones in earthquake-prone areas in Greece, Italy, and Switzerland [1].

Radon measurements in air or soil often have substantial uncertainties due to natural background variations and large distances from epicenters. The ArtEmis project aims to address these issues by using many sensors for high spatial resolution, conducting real-time measurements in groundwater, and applying advanced data analysis with machine learning algorithms. A particularly interesting radon measurement in groundwater was performed before the Kobe earthquake in 1995 [2]. A well at 17 m depth showed a clear radon increase 9 days before the 7.2 magnitude quake, peaking one week prior. In contrast, a shallower well at 4 m depth did not show changes. Seismologists at Kobe used advanced radon detectors developed by the Kamiokande neutrino experiment team in Japan. The Kamiokande experiment also recorded a radon increase 2.5 days before a 3.9 magnitude earthquake, 45 km away, from a mine 1000 m underground [2].

ArtEmis also aims to improve earthquake forecasting. While long-term statistical forecasts are possible, precise predictions of the exact time and location are not. The connection between the radon concentration precursor and the consequent earthquake has been observed and studied in the past [1]. Radon from uranium decay is common in deeper earth layers. Increased stress along fault zones creates new cracks, raising radon emission rates in areas several times larger than the earthquake's rupture length. During interseismic periods, radon emission remains constant. As an earthquake approaches, stresses increase, forming many cracks and emitting more radon. The final rupture occurs in the area of the highest stress and radon emission. Radon reaches the surface through carrier gases (like CO_2 and methane) or water, depending on the geological structure of each site. This means that each well in the ArtEmis project may have unique conditions. Some wells, such as the shallow one near the Kobe earthquake, might not show radon variations during earthquakes. Identifying the best wells for the project remains an open issue and requires ongoing observation. However, by conducting measurements across many wells, the project aims to balance the varying conditions at individual sites. ArtEmis covers a wide geographical area with dense measurements in test sites and frequent smaller earthquakes.

Establishing firm relations between measurement sites and subsequent earthquakes will take longer than the project's duration. Therefore, plans are in place to prolong and expand the project. To achieve a relevant statistical significance, a sensor density of approximately one every 100 km^2 could possibly be reached; however, the ArtEmis project will provide more information about the optimal distribution of sensors since it may depend on the local region.

As stated in [3], considering observed precursor phenomena within a specific circular area of radius ρ, one possible simplified relation between the magnitude M of an earthquake and the distance ρ to the epicenter is

$$\rho = 10^{0.43M} \text{ km} \tag{1}$$

or in a more general form, as suggested in [4]:

$$D = ae^{M} \tag{2}$$

Equations (1) and (2) show that the more powerful the earthquake, the larger the radius where precursor phenomena can be observed. The ArtEmis project will give insight into the parameters. Those relations will also be used within the machine learning model, which will be developed by a horizontal group to verify the potential of radon and other measured quantities as relevant and reliable precursors.

1.2 Purpose

This thesis investigates some parameters of the radiation physics of the chosen sites for the ArtEmis project through Monte Carlo simulations using the software package Geant4. It gathers useful results for future contributors and provides preliminary findings to guide the project's development.

Although the detection of gamma radiation underwater is a well-known topic, in the particular application of the studied sites of the ArtEmis project, it is not completely clear how detector geometry and distance to the walls will affect the measurement. From the theory, which will be described in one of the following paragraphs, it is known that radiation from a source placed in water will have more difficulty reaching the detector, and most of the gamma photons will be scattered several times during their path, decreasing their energy. So, the expected gamma spectra detected in water will look different than in air, and the effect of radioactive nuclides inside a wall will depend on the distance from the detector. Such topics, as many others related, will be investigated in this thesis in order to find valuable results.

1.3 Delimitations

A critical point of the ArtEmis project, which also influences the thesis results, is the correct operation of the detectors. It can be seen in the recorded data transmitted by the electronics at the site that many detections fail or are not correctly transmitted, even if the reason is not fully clear. The influence of this limitation will be explained in one of the following sections. Another criticality is that the software package used for the simulations, Geant4, does not allow the simulation of time dependence. So, the full decay chain of the simulated nuclide is instantaneous, and all the particles from each decay are emitted simultaneously. This is not the case in real phenomena, where every decay has a mean time range before it occurs. However, this can be intended to approximate an equilibrium situation, in which every nuclide has a concentration

constant over time. Due to the simplifications and the non-ideal conditions, the results of this study are not likely to be very similar to the actual situation, so they have to be considered good indicators for understanding the behavior of the real sites and the project's future development. Moreover, the calibration performed in section 3.5 with the available data will be shown to be unsuitable for the study of the actual spectrum.

1.4 Method

To study the real sites where the detectors have been placed for the ArtEmis project, it is necessary to know each one's setup, which is different, and define the relevant parameters for the computer simulations. This thesis's work was primarily conducted using Geant4, a software package developed by CERN.

1.4.1 Geant4

Geant4 (GEometry ANd Tracking) includes many different physics models to manage particle interactions with matter over a vast energy spectrum. It integrates data and expertise from numerous global sources, effectively serving as a repository comprising a significant portion of knowledge on particle interactions. It is often used in particle physics, nuclear physics, detector design, nuclear medicine, radiological equipment design, and many other fields. Geant4 is implemented in C++ and uses advanced software-engineering techniques and object-oriented technology. For instance, it separates how cross-sections are input or computed from how they are used or accessed, allowing users to customize both [5].

The most important features of the simulations for this thesis are the geometry construction and the definition of the materials. The domain is formed by a so-called “world”, the environment in which the simulation is performed, and everything is built inside it. For each element placed inside the world, it is possible to define the material, properties, and geometric dimensions. Geant4 does not allow the simulation of time-dependent phenomena, which could seem a significant limitation for this thesis since the main physical phenomenon is radioactive decay, which is time-dependent. However, the program simulates an instantaneous decay chain, which is a good approximation for an equilibrium situation where the concentrations of all the daughter nuclides of radon are constant.

To simplify the program's setup for the simulations, a virtual machine, VirtualBox, has been used to install Geant4 and run the macro files. The simulated operating system is Ubuntu version 20.04.6, installed in Windows 11.

1.4.2 The g4sds program

The g4sds (geant4 sample detector simulation) program is a code written with Geant4 by professor Johan Nyberg at Uppsala University. Its purpose is to simulate a sample, a detector, and a source emitting radiation. It was developed using rdecay02 as a starting point, a program that is one of the example programs included with the Geant4 source code. This program permits one to create a parallelepiped-shaped world with variable side lengths and choose the medium material. A sample can be inserted, possibly choosing between a box and a cylindrical shape, the geometrical dimensions, and its material. Creating a container made of a different material for the sample is also possible. Then, inside the code, it is possible to build the detector, defined by the crystal made

of a chosen material, a dead layer around it, a capsule, and a detector shield. Also, an absorber can be placed inside the world domain with chosen dimensions and position. Then, regarding the detector, the *Full Width Half Maximum* (FWHM) parameters for the peaks of the resulting spectra are set to consider the crystal material resolution. Every material has different parameters, and resolution is energy-dependent so that the FWHM can be defined through equation (3),

$$FWHM = \sqrt{f + g \cdot E_{det} + h \cdot E_{det}^2} \tag{3}$$

where f, g, and h are the FWHM parameters, while E_{det} is the energy deposited inside the detector. The so-called *General Particle Source* (gps) defines the radiation source. With the gps it is possible to define the ion by its atomic number Z, atomic mass A, and ion charge Q. The source can be set as a point, plane, beam, surface, or volume, and its position and dimension can be changed. The number of simulated decays can be decided depending on the source's activity and the detection time.

1.4.3 On-site measurements

In the frame of the ArtEmis project, many sites have been identified as good spots to perform the required measurements for the studies. The choice of the sites is mainly based on the seismicity and the radon activity of the places because they are the most relevant parameters for the study's success. Seismicity is a key point because one of the final goals of the ArtEmis project is to acquire further data from the occurrence of a seismic event. A high radon activity is important for having useful results in the detected spectra.
The chosen sites are in Italy, Greece, and Switzerland, each with a different setup, depending on the territory's characteristics. The detectors and the auxiliary electronics used have been chosen through a cost-benefit analysis, which led to the adoption of CsI scintillator detectors. The most relevant site will be described in Chapter 3.

1.4.4 Detectors

Several detectors at the chosen sites perform the measurements needed within the ArtEmis project. All of them are "scintillators", a type of detector composed of a scintillating material followed by a photomultiplier. A scintillator is a material that emits light when it is hit by ionizing radiation [6]. This light can then be exploited to produce an electric signal through electronic devices. Many different materials are used today for detecting ionizing radiation; some are organic crystals and liquids, plastic materials, gases, or glasses. However, the most well-known scintillator type is inorganic crystals, such as NaI or CsI, with sometimes the presence of impurities like thallium. This scintillator type is particularly good because it shows high efficiency and good energy and time resolution. The different types work in various ways, but the starting point is always the excitation of the material's electrons, with the emission of a photon after the de-excitation. The scintillator is transparent to the emitted light wavelength to permit its extraction.

The photomultiplier (PM) is usually in direct contact with the scintillator or connected through a light guide. It is composed of a tube filled with a thin layer of a material called a photo-cathode, which converts the light photons into electrons by the photo-electric effect. The electrons produced this way hit the first of a series of electrodes, also called *dynodes*. There is an electric potential of about 100 V between each pair of them, so if an electron hits a dynode at an energy corresponding to the potential difference, it will release more electrons, creating a multiplying process.

However, the detectors used in the ArtEmis project are quite different because they are coupled to so-called SiPMs, which are not traditional photomultipliers. In fact, SiPMs are based on single avalanche diodes (SPADs) implemented on a silicon wafer, with dimensions of 10 to 100 micrometers and a density of up to 10000 per square millimeter [7].

2 FRAME OF REFERENCE

The ArtEmis project aims to investigate the detection of radon in water in order to use it as a precursor to predicting earthquakes well in advance. This is justified by empirical observations made in the past. The first observation of an increase in the groundwater radon concentration preceding an earthquake dates back to 1966, during the days before the seism in Tashkent, current Uzbekistan [2]. During the following years, many monitoring studies and reports were created, in particular by Japanese scientists. In 1994-1995, a detector system for monitoring groundwater radon was operated in Japan, but the Kobe earthquake, which occurred on the 17th of January 1995, caused the detection chamber to collapse. A few months earlier, by November 1994, the measurements showed a radon activity three times higher than the stable reference level of 20 Bq/l, and then a sudden peak on January 7th, 1995, followed by a decrease during the seven days before the earthquake, which had a seismic moment magnitude of M_w=6.9.

Between April 2017 and December 2019, in the Apennines region in Italy, a study of the measurements of two different springs was carried out concerning normal seismic activity and in connection to events of seismic moment magnitudes $M_w \geq 3.5$. Before the M_w=4.4 Balsonaro earthquake on November 11th, 2019, radon levels increased twice: 500 Bq/m³ (10% above average) 17 days prior and 1500 Bq/m³ (8% above average) 11 days prior. Elevated radon levels also preceded the M_w=3.8 L'Aquila earthquake on the 31st of March, 2018, with an increase of 1200 Bq/m³ (7% above average), and the M_w=3.9 San Leucio del Sannio earthquake on December 16th, 2019, which showed an upward trend of 1000 Bq/m³ (20% above average) in November. Similar earthquakes without these radon increases were attributed to geological factors. Overall, the results are promising.

In the frame of the ArtEmis project, much work was done before the present study. Since the project covers many fields, different students and professors have contributed, from geological studies to detector electronics, the transmission and processing of signals, and simulations. Among them, useful results and information used in this study are taken from the work of Gururaj Kumar [8], Patryk Törngren [9], and Maja Walfridson [10]. In particular, the last student performed a study of an ArtEmis-like setup, which is mainly focused on investigating the effects of a ^{137}Cs source placed on the wall of a water tank and a detector placed inside the water.

2.1 Earthquakes prediction

An earthquake is the result of the elastic recoil from the movement of the crustal blocks caused by the thermal and gravitational convection in the mantle beneath [11]. The relative movement of blocks from each other in a horizontal direction is called a strike-slip; in the case of one block going down over another, it is called normal faulting; when a block is moving up, it is called reverse faulting or thrust. The proper evaluation of earthquake energy is performed by introducing the concept of magnitude. It is defined as the decimal logarithm of the maximum amplitude, measured in microns, recorded by a standard Wood–Anderson seismograph 100 km from the epicenter [12]. It is also called local magnitude and can be calculated as in equation (4),

$$M_L = log_{10}A + 2.56log_{10}\Delta - 1.67 \quad (4)$$

where A [μm] is the *waveform amplitude*, Δ [km] is the *distance* from the seismograph to the epicenter. The formula is valid for values of $10 < \Delta < 600$ km.

Different waves can be generated during an earthquake: volumetric (longitudinal P-waves and shear S-waves) and surface waves (Rayleigh waves and Love waves) [11].

Although big efforts have been put into research to find a reliable method to forecast earthquakes days or hours in advance, no technique exists nowadays [13]. Predicting an earthquake means understanding the time, place, and magnitude of its occurrence, and the forecast can be classified, depending on the time scale, into long-term (decades), medium-term (years), or short-term (months, weeks, or hours). The attempts to study this topic can be divided into probabilistic and deterministic. The former is based on the studies of the geology of an area and its seismic history [14,15], while the latter is based on the physical precursors and the actual occurrence of seismic events [16].

2.2 Radon origin

One of the most critical contributors to natural background radiation is the radioactive decay of naturally occurring radionuclides. Among them, the radioactive families of uranium (U) and thorium (Th) and the radioactive isotope of potassium (K) are responsible for most of the dose to humans.

Uranium is a heavy element with atomic number 92. In nature, it occurs with two main isotopes, ^{238}U, with an abundance of about 99.3%, and ^{235}U, with an abundance of 0.7%, both of which are radioactive but with different half-lives [17]. The first has a half-life of 4.5 x 10^9 years, and the second is 7.0 x 10^8 years. A much less abundant isotope is ^{234}U (0.0056%), with a half-life of 2.4 x 10^5 years; it is the third decay product in the ^{238}U radioactive decay series. Uranium is present in many forms on Earth's surface. It is dissolved in seawater, with a concentration of 3.3 ppb, due to its solubility, but it is also present in different concentrations inside rocks and minerals [18]. The isotopes ^{235}U and ^{238}U both undergo a decay chain, but the former ends up in ^{207}Pb while the latter is in ^{206}Pb, as shown in Figure 1 and Figure 2.

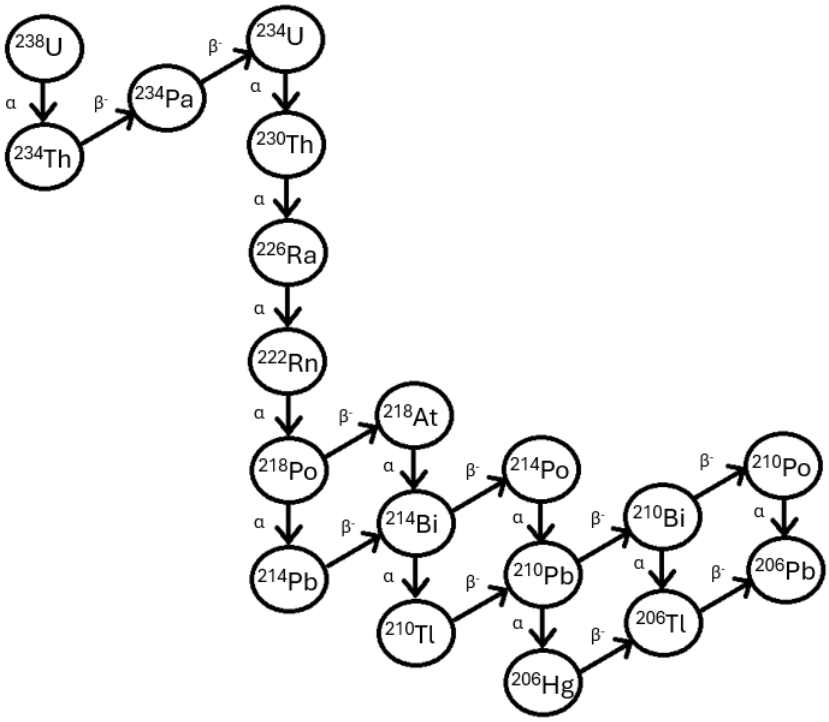

Figure 1. Decay chain of ^{238}U.

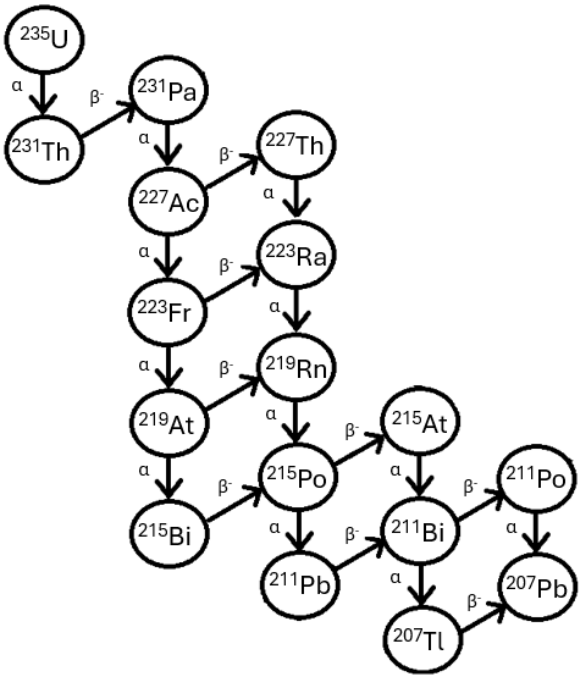

Figure 2. Decay chain of ^{235}U.

Thorium, instead, has atomic number 90, and 99.98% of the total mass on earth is isotope ^{232}Th, which has a half-life of 1.41 x 10^{10} years. It is mainly present in rocks and minerals of the soil [17]. Figure 3 shows the thorium decay chain, ending in the stable isotope ^{208}Pb.

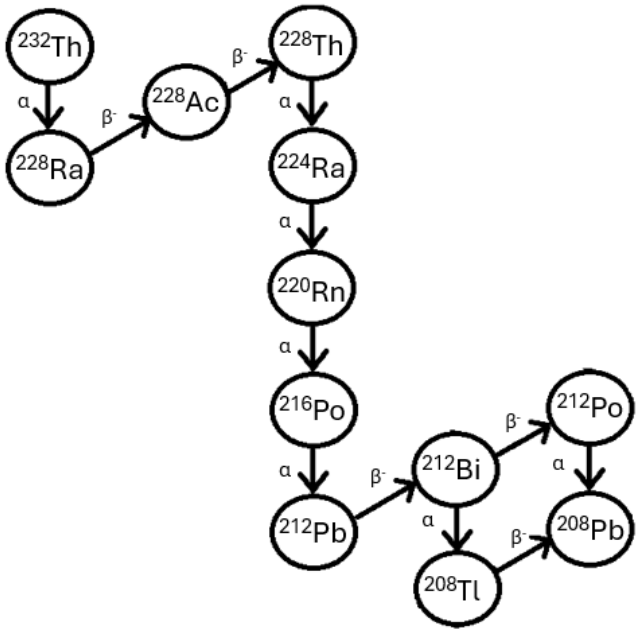

Figure 3. Decay chain of ^{232}Th.

Potassium has atomic number 19 and three natural isotopes, two stable (^{39}K and ^{41}K) and one radioactive (^{40}K) [17]. The most abundant is ^{39}K, which constitutes 93.3% of the total potassium mass; the second is ^{41}K, which accounts for 6.7%; and the third is ^{40}K, which is 0.0117%. The radioactive isotope has a half-life of 1.248×10^9 years and can undergo both a beta decay and an electron capture. In nature, potassium can be found mostly in many igneous and metamorphic rocks and some chemically precipitated sedimentary rocks, but also in different concentrations of minerals, organic matter, living organisms, water, and air.

Within the scope of this report, the most relevant element is radon (Ra), a radioactive noble gas. In nature, it exists in three isotopes: ^{222}Rn, ^{220}Rn (also called Thoron), and ^{219}Rn. The most stable and abundant is ^{222}Rn, formed during the decay chain of ^{238}U, shown in Figure 1, and has a half-life of 3.82 days. The second most abundant is ^{220}Rn, a short-lived isotope with a half-life of 55.6 seconds, formed in the decay chain of ^{232}Th.

2.3 Geology of radon

Radon is formed inside the rocks where uranium and thorium are present; however, since it is a noble gas, it is very likely to migrate through the ground according to its permeability, eventually reaching air or water. In particular, since ^{222}Rn is a member of the ^{238}U decay chain, its presence in rocks and soil depends on the uranium content [17]. Average uranium concentration varies from the lowest in sedimentary rocks to the highest in magmatic rocks. However, uranium can be found in uncommon concentrations in all rock types as impregnations in sedimentary deposits or vein-type deposits in metamorphic or magmatic rocks. In order to determine uranium concentrations, the methods used are usually based on gamma-spectrometry over large areas, fields, or laboratory gamma spectrometry on solid samples (such as soils and rocks) or liquid samples (such as water), for detailed studies or calibration of airborne measurements. Radiometric data have some limitations due to the differences between airborne and ground gamma spectrometric data, regional and detailed geological mapping differences, and the presence of factors influencing radon migration and diffusion from deeper soil to the surface and subsequently to dwellings.

The permeability determines the transport of radon and other soil gases, while the emanation coefficient characterizes the production of radon in mineral grains. Permeability, defined by Darcy's Law, indicates how easily fluids can pass through a porous material, with units of m² or darcies. Permeability is crucial for assessing radon risk, as high permeability in the soil beneath buildings can lead to significant indoor radon levels, even with low soil radon concentrations. Various factors, including soil moisture, texture, and environmental conditions, influence permeability and must be considered to assess soil gas movement accurately. It is necessary to specify the distinction between micro- and macro-permeability; the former is related to the porosity of the soil, while the latter is related to the fissures and cracks formed inside the rocks.

Radon diffusion occurs in pore space through the connections between mineral grains and is controlled by physical conditions such as temperature, pressure gradients, or soil moisture. Moreover, it can be both vertically and laterally oriented. Sub-horizontally oriented mineral particles (like micas) or layered clay intercalations in soils or clayey weathered rocks can be an obstacle to the vertical migration of the soil gas and can trigger lateral convection. Currently, permeability is usually determined through in situ measurements, soil texture analysis, and data from soil permeability maps (generally available at a regional level, so they cannot be used for local estimation).

The emanation coefficient, instead, is a parameter that describes the movement of radon in the soil. Still, in most papers on the transfer of radon, the physical meaning of this parameter is not disclosed, and the methods of their determination are not justified [19]. Moreover, simulations

often use the values obtained under laboratory conditions, where the atmosphere influence is negligible.

Since radium and uranium have different solubility in groundwater, the local radon production rate is not necessarily in equilibrium with uranium (or thorium) at the same point in the ground, thus promoting the migration of the gas [17]. However, most of the radon inside rocks doesn't reach air or water because the migration is quite slow, depending on the porosity of the rock and the grain size. The movement of radon atoms is determined by the water content of the soil (since radon diffusivity is lower in water than in air), permeability, pressure difference, concentration differences, and the presence of other carriers such as CO_2 or methane. Since radon is soluble in water, it can be transported through dissolution over large distances and released if the solubility conditions change. Alternatively, radon can be generated by the decay of radium dissolved in the water and flow to the atmosphere.

Several factors control radon concentration in the soil, both on daily and seasonal scales. Soil-gas radon levels are controlled by precipitation and temperature on a seasonal scale. In contrast, barometric pressure, temperature, soil moisture, and wind affect radon concentration and behavior on a smaller time scale. To predict radon concentration on a longer time scale, it is necessary to know the interaction between these climatic variables and perform statistical analyses. Furthermore, soil gas surveys cover large areas with different rock and soil characteristics. Hence, a deep knowledge of the geology and the soil affecting radon generation and transport is necessary.

Geological and man-made inhomogeneities can also influence the radon concentration in soil because they are more permeable and intersect more rock types with different radon potentials. Different types of faults primarily represent geological inhomogeneities, and the radon migration velocity and its concentration in shallow soil are mainly due to the distance to the fault plane and the bedrock lithology. The fault geometry and activity and fractured rock volume affect the spatial distribution of radon concentration because radon peak values can assume different spatial positions within the fault zone. Radon anomalies can have various intensities and shapes, and they are distributed in faulted areas with a connection to the evolution of the fault zone. The thin core of the faults serves as a convective pathway for radon flux upwards; thus, in the damage zone surrounding the fault core, radon can be released with a more significant flow, namely when the fault core is impermeable. The man-made inhomogeneities derive from human activities in old mines, where the soil-gas geodynamics of underground spaces can be transposed to the superficial layer through the pits, abandoned adits (even if backfilled with inert material), or through fissures in case of subsidence areas. Inside the Earth's crust, radon concentrations usually increase with depth, depending on the type of rocks, because of the local differences in soil layers and bedrock lithological types. Moreover, since there are roots of vegetation disturbed by the disintegrated soil particles at the surface layer, the radon concentration tends to be diluted in contact with atmospheric air. The measured concentrations in the soil usually range between 5 and 100 kBq/m^3, but they can reach tens of thousands, depending on the type of rocks. Instead, in the atmosphere just above the soil, they only reach tens of Bq/m^3 and up to hundreds [20].

Both geological and meteorological parameters can affect the physical processes of radon generation in the soil [17]. So, radon concentrations measured in summer cannot be used to predict radon levels in winter; this is the reason why soil-gas surveys are usually carried out in a short time and during stable weather conditions. According to the literature, the main factors affecting radon concentration in rocks are soil moisture retention characteristics (such as permeability, porosity, grain size, and the number of consecutive rainy days), barometric pressure, soil temperature, hydrometeors occurrence (mainly snow and ice), and wind velocity.

Moisture in soil pores is another factor influencing the radon concentration. The increase in moisture content reduces the soil permeability and the availability of air in pores, with a consequent increase in radon concentration. This occurs because radon has a high solubility in water and a less diffusive mobility in water than in air, so it accumulates. Radon variability due to

humidity is related to water saturation and the moisture retention characteristics of the soil. In highly permeable soils, increased humidity reduces air permeability in the pores, hindering radon transport and increasing its concentration in the soil. Rainfall increases the concentration of radon in the soil immediately after the event. During the rainy seasons (winter and spring), the radon concentration can increase due to the formation of a layer of soil saturated with water, which reduces gas permeability. During the dry seasons (summer and autumn), radon is released more efficiently since the soil is drier and more permeable.

The presence of snow and ice on the ground causes the accumulation of radon due to the "capping" effect, which limits the escape of gas from the ground. Similarly, barometric pressure has a significant impact on soil-gas radon concentration, exhibiting an inverse relationship even in the absence of precipitation. Changes in barometric pressure generally result in smaller variations in radon compared to changes in soil moisture. Decreasing pressure pulls soil gas out, raising near-surface radon levels, especially in permeable soils where radon escapes quickly into the atmosphere, reducing concentration at depths of 0.6-0.8 meters [21, 22, 23]. Increasing pressure pushes atmospheric air into the soil, diluting near-surface radon and driving it more profoundly. Pressure changes of 1-2% from weather fronts can lead to 20-60% changes in radon flux, influenced by the rate and duration of the pressure change [24].

Temperature has a different impact on soil-gas radon concentrations compared to barometric pressure [17]. Its effect is generally minor relative to precipitation and barometric pressure. Lower air temperatures may correlate with higher radon levels, but this effect diminishes below 0.6 meters in depth. Temperature differences between soil and air can cause thermal convection, moving soil gas vertically. Soil temperature increases can boost radon levels by enhancing radon mobility and gas carrier production (like CO2 and water vapor). High summer soil temperatures can raise radon concentrations by 14% compared to winter [25]. Frozen upper soil layers can trap radon in colder seasons, leading to higher indoor levels [17]. Temperature and barometric pressure can amplify radon flux from soil to atmosphere, causing temporary radon imbalances.

High wind speeds cause local depressurization, reducing soil radon concentrations by diluting the gas with atmospheric air or removing it at the surface. Wind effects are noticeable up to 1.5 meters deep [22, 23]. Factors like soil permeability, moisture, and ground cover (e.g., snow or ice) influence the extent of wind's impact [17]. Strong turbulence and the Bernoulli effect can draw soil gas upward through pressurization and depressurization cycles, similar to the effects of barometric pressure.

2.4 Radiation and particle interactions

The knowledge about interactions and effects of radiation passing through matter is of paramount importance for the experimental applications of nuclear physics, and it is the basis of the functioning of all particle detection devices [26]. Such reactions occur at an atomic or subatomic level, depending on the type of radiation, its energy, and the type of material. They are governed by the laws of quantum mechanics and the relative strengths of the forces involved. So, for charged particles and photons, most of the processes are governed by electromagnetic interactions since the relative strength and range of the Coulomb force are much higher compared to the other interactions. Instead, for neutrons, strong interactions most probably occur, even though electromagnetic and weak processes are not negligible.

The concept of cross-section generally describes the probability that a reaction will occur between two particles. This probability can be calculated if the form of the basic interaction between the particles is known.

The fundamental interactions between particles are the key to understanding the output of gamma detection. To explain the shape of a gamma spectrum, it is necessary to know the physical processes involved in the gamma photons' travel through the matter. The most relevant phenomena for the already explained purposes are the *photoelectric effect*, *Compton scattering*, and *pair production*.

2.4.1 Photoelectric effect

In the phenomenon called *photoelectric effect*, the photon hits an electron and transfers all its energy, disappearing in the process [26]. Let's consider the electron initially at rest, after the collision. It will travel in the same direction as the incident gamma photon, considering that part of the transferred energy is needed to overcome the electron's binding energy. This is the reason why, in a gamma detector, the energy of gamma rays undergoing this process is characterized by a peak, called *photo peak*, which is discrete. This is very important for studying the physics covered in this thesis.

2.4.2 Compton scattering

Compton scattering is more probable at higher energies. In this process, the gamma photon transfers only part of its energy to the electron [26]. After that, it scatters in another direction with a lower energy, while the electron will travel with the new energy in a direction that conserves the linear momentum of the system. So, after depositing part of its energy in the material, the gamma photon could also leave the material. Inside a detector, there is a statistical distribution of the deposited energy, which can be visualized in the gamma spectrum as a continuous distribution at energies lower than the total initial photon energy. This is one of the main processes of interest for this thesis. The complex nature of the Compton multi-scattering makes this physical phenomenon especially suitable for the simulations performed with Geant4

2.4.3 Pair production

The process of pair production is relevant for even higher energies. It consists of an interaction between the gamma photon and the electromagnetic field of the atomic nuclei, and the result is the production of an electron and a positron. However, to allow the creation of these particles, the photon's energy must be higher than the sum of the mass-energy of the two, which is 1022 keV, and the remaining energy is converted into the kinetic energy of the two particles [26].

2.4.4 Radon decay

As previously explained, radon is part of the natural decay chains of uranium and thorium; in particular, the most relevant isotope, ^{222}Rn, is part of the ^{238}U chain [26]. It decays into ^{218}Po through alpha decay, with a Q-value of 5.590 MeV and a half-life of 3.822 days. The following decays of the chain, from ^{218}Po to the stable ^{206}Pb, are both alpha and beta, with the emission of some gamma photons. The last mentioned are those detected with the sensors used in the ArtEmis project to give the gamma spectra. The other isotopes are ^{220}Rn and ^{219}Rn. The former is created in the decay chain of ^{232}Th and undergoes an alpha decay, with a Q-value of 6.405 MeV and a

half-life of 55.6 seconds. The latter is a daughter nuclide of the ^{235}U decay chain and decays into ^{215}Po through alpha decay, with a Q-value of 6.946 MeV and a half-life of 3.96 seconds.

3 IMPLEMENTATION

After analyzing all the sites of the ArtEmis project, only one was chosen as the most relevant and fit to perform the studies of this thesis. At the time of writing, eight sites had been chosen to place the ArtEmis sensors at Gran Sasso, Italy, as shown in Figure 4, although only three were provided with detectors. In this work, the focus is on the installation at site 3.

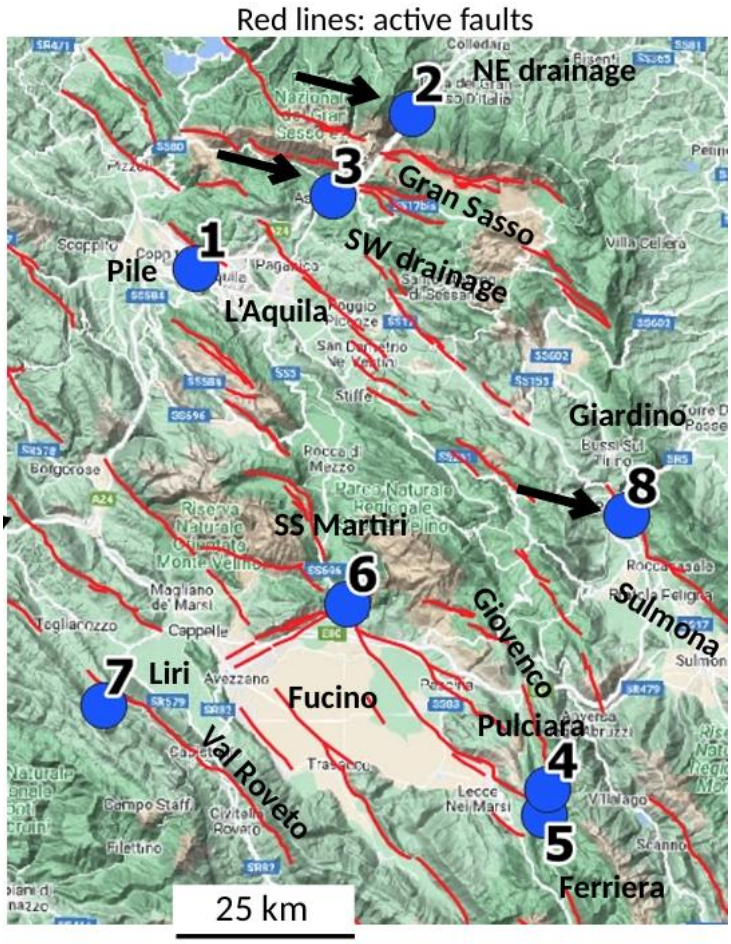

Figure 4. Map of the ArtEmis sites in Italy, Gran Sasso.

The geometry is shown in Figure 5, where the red square is the domain considered for the simulations, which are described in the following paragraphs. The detector is placed inside the water pool and connected to the transmitter unit, which is linked to the gateway. This electronic setup is needed for data collection and transmission, but it will not be included in the simulations.

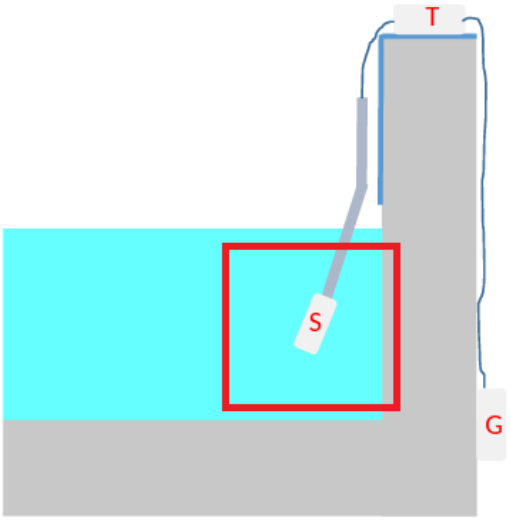

Figure 5. Scheme of site 3 in Italy with the domain of the simulations highlighted in red.

The tube connected to the sensor is inclined by 13° in order to place it at a proper distance from the wall, at a depth of ≈2 meters from the surface of the water. In this geometry, the detector sits at a distance of 46 cm from the concrete wall. The world of the simulation is a cube of water with the detector placed in the center, and a wall made of concrete on one side, as shown in Figure 6, where simulated gamma photon trajectories are also present.

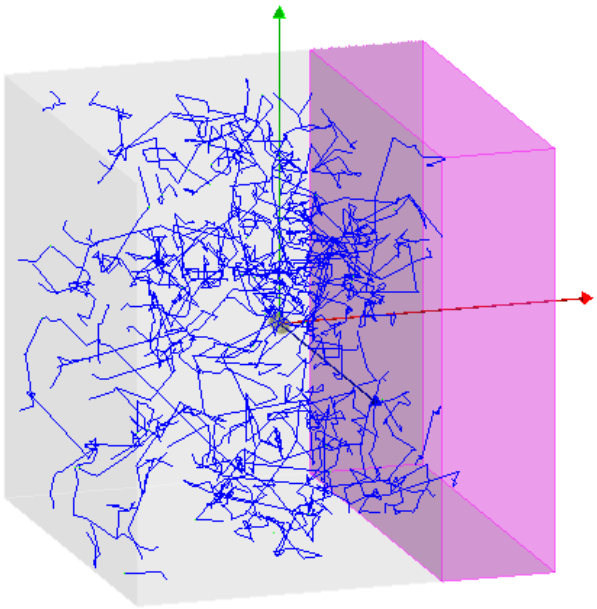

Figure 6. Geometry of the domain of the main simulations with the trajectories of some particles. The pink sample is the concrete wall.

The presence of the wall in the simulation's geometry is essential because the sensor detects radiation from both the radon in the water and the potassium in the concrete.

3.1 Energy deposited in the world

The most relevant output of the simulations of this thesis is the gamma spectrum detected in the simulated sensor, which has an energy range from 0 to 4095.5 keV. However, with the g4sds program, it is possible to see the spectrum of the energy deposited in the world of the simulated domain by the particles produced in the decays, looking at higher energies. So, it is interesting to investigate this spectrum to understand better the physics of radon decay in air and water and how it is elaborated in Geant4. For this purpose, two simulations were performed, one with ^{222}Rn decaying in the air, which is set as the world material, and the other with the same nuclide decaying in water. The geometry of both simulations is composed of a cube with a side length of 2 m, which is the world, made of air or water, and a detector placed in the center, with a volumetric source of ^{222}Rn undergoing decays. The detector is formed by a cylindric crystal made of CsI, the scintillator material used in this case, with dimensions 4 cm as radius and 8 cm as length. The whole geometry is shown in Figure 7.

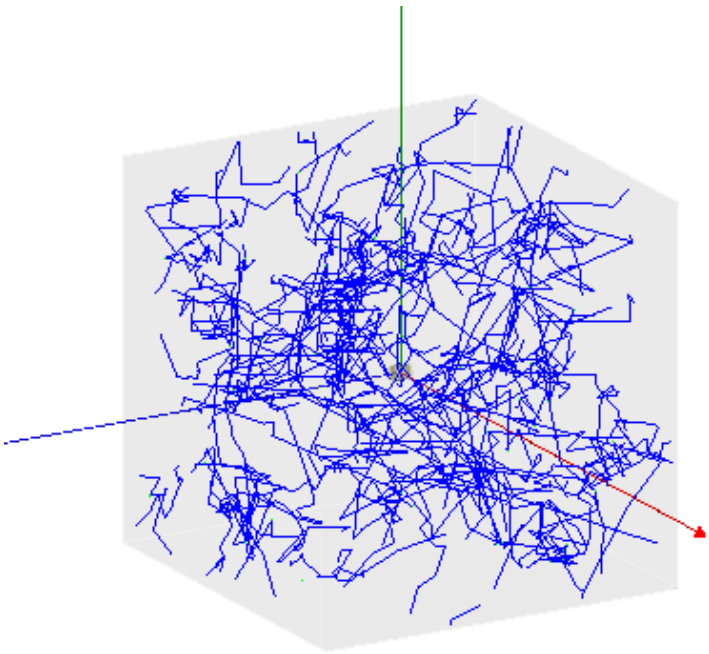

Figure 7. Domain of the simulations for determining the energy deposited in the world

3.2 Domain dimensions

Looking at the physics of the gamma photons detected in the sites, it can be noticed that, in the absence of obstacles, after a certain distance from the detector, the particles emitted from the radioactive decays cannot reach it anymore due to the much more probable interaction with the medium. This raises a question about the domain size to be used in the simulations to exclude that irrelevant and redundant part, which would consistently increase the computing time. So, several simulations have been conducted with a constant number of events per cubic meter and a cubic domain with increasing side lengths, with the choosing criteria that the relative difference between

the detected particles in two consequent simulations must be sufficiently low. The relative difference is calculated through equation (7),

$$rel.diff. = \frac{|N_2 - N_1|}{N_2} \quad (7)$$

where N_1 and N_2 are the total numbers of detected events of two consecutive simulations.

This process has been done with two different media, water and air, and the geometry of the simulations is represented in Figure 8 and Figure 9,

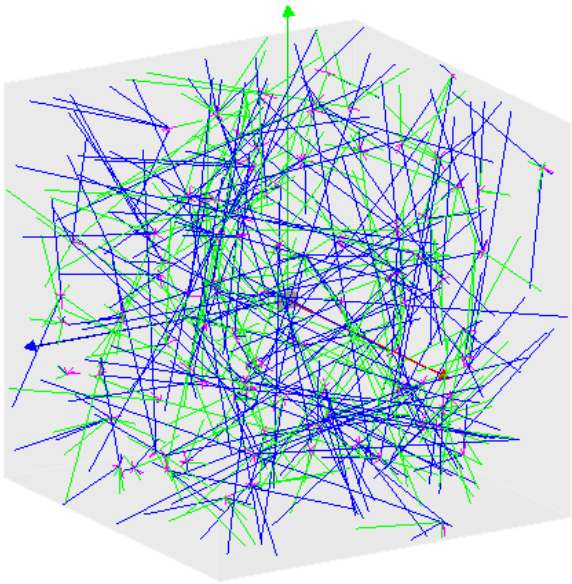

Figure 8. Representative geometry of the simulation for determining the domain dimension with air as world material. Gamma photons are in blue, beta electrons in green, and alpha particles in magenta.

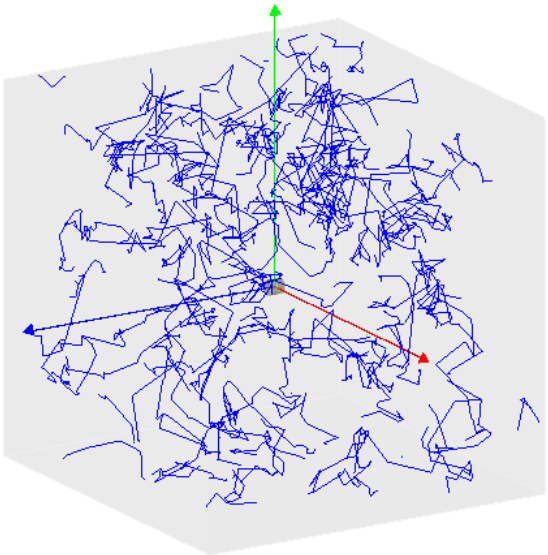

Figure 9. Representative geometry of the simulation for determining the domain dimension with water as world material. Gamma photons are in blue, beta electrons in green, and alpha particles in magenta.

where also 100 simulated events are shown. In the geometry with air, it can be seen that gamma photons (in blue) are more complimentary to travel. At the same time, beta electrons (in green) and alpha particles (in magenta) are not even visible in the geometry with water because the medium immediately stops them. The density of the medium influences the path of particles. In particular, for gamma photons, it can be seen in equation (8),

$$I(x) = I_0 \cdot e^{-\mu x} \tag{8}$$

where I(x) is the *intensity* of a beam of gamma rays as a function of the distance x, I_0 is the *initial intensity*, and μ is the *gamma absorption coefficient* or *linear absorption coefficient* [6]. In particular, the value of μ for a specific energy is easily deduced by the relationship in equation (9),

$$\mu = \left(\frac{\mu}{\rho}\right) \cdot \rho \tag{9}$$

where $\frac{\mu}{\rho}$ is the *mass attenuation coefficient*, which can be found in published tables from databases such as NIST [27], and ρ is the density of the medium. Another coefficient, similar to the linear absorption coefficient, is the *mass energy absorption coefficient*, $\frac{\mu_{en}}{\rho}$, used for calculating the energy deposited in a material by a beam of photons (called the dose).

These two coefficients depend on the photon energy, and this dependence can be seen in Figure 10 for water and Figure 11 for air.

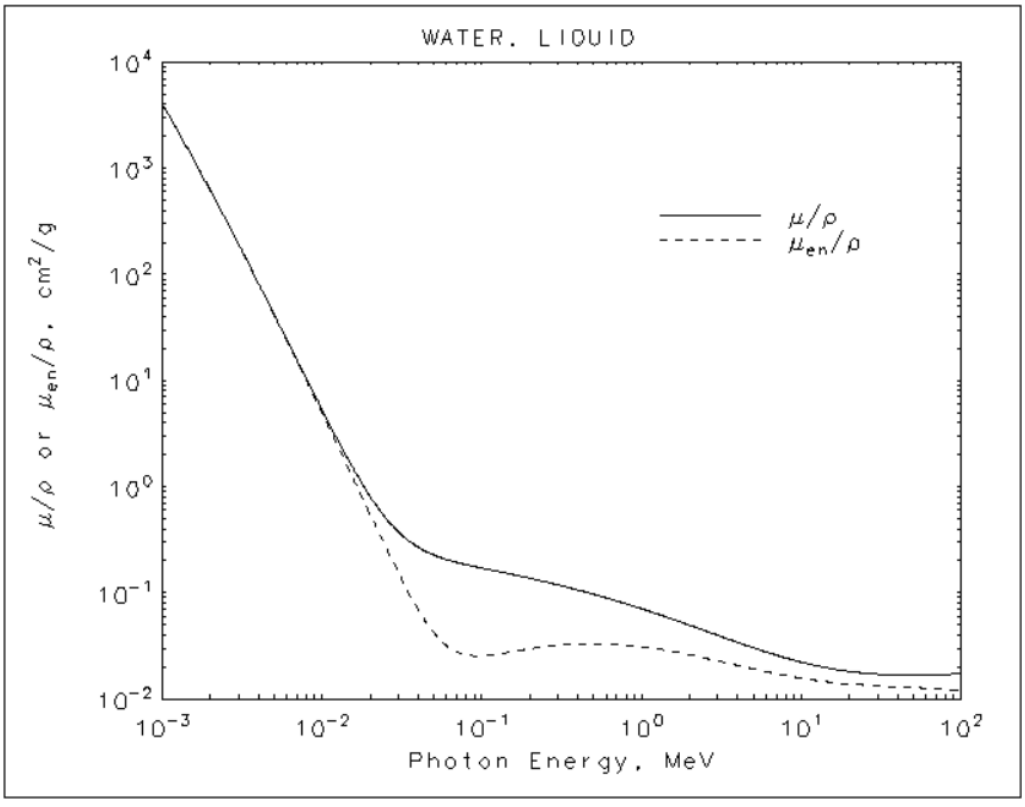

Figure 10. Plot of the mass attenuation coefficient (continuous line) and mass energy absorption coefficient (dotted line) in water from NIST [27].

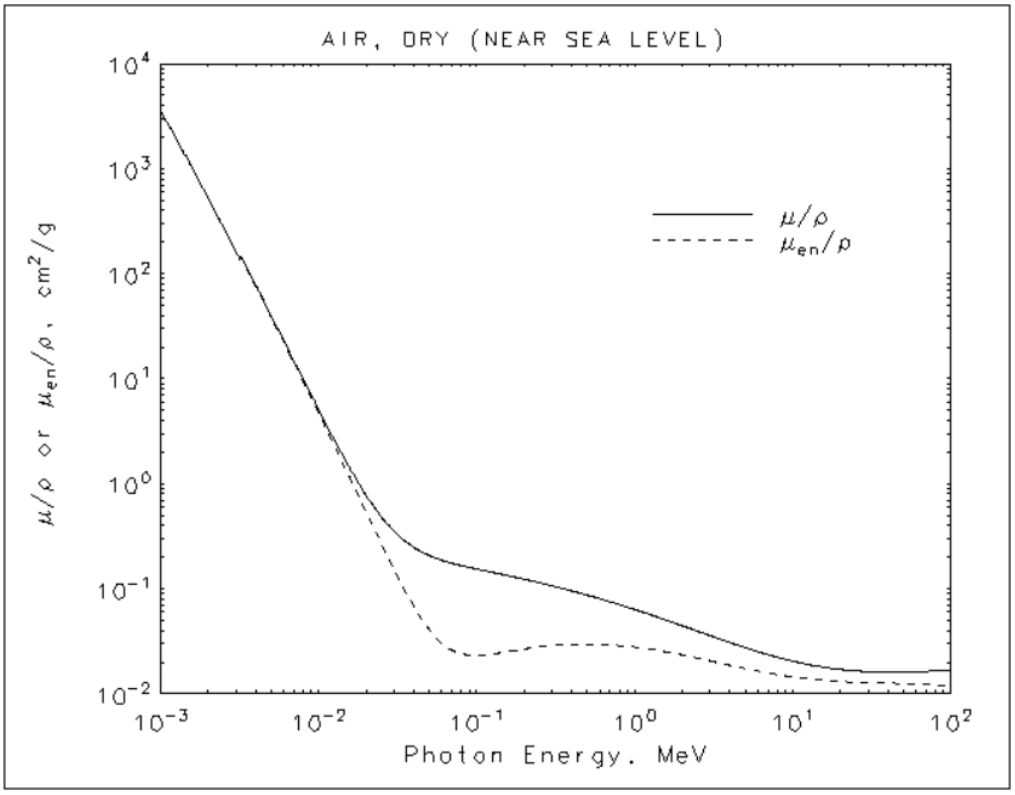

Figure 11. Plot of the mass attenuation coefficient (continuous line) and mass energy absorption coefficient (dotted line) in air from NIST [27].

3.3 Effects of the distance from the wall

One of the main interests in studying the real site is to simulate the interferences that could affect radon detection. So, many simulations have been performed to investigate the effect of the ^{40}K in the wall on the gamma spectrum with different concentrations of the radon in the water since this is the earthquake precursor studied in the frame of the ArtEmis project, considering different distances between the wall and the detector and different quantities of radon in water (which means different radon activities). The simulations were performed considering three different K_2O concentrations in the wall, three radon activities in water, and three wall distances from the detector, all shown in Table 1.

Table 1. Parameters of the simulations.

K_2O concentrations (%)	Radon activities (Bq/l)	Wall distances (m)
0.12	4	0.05
1.2	40	0.35
12	400	0.75

The concentration of K2O is chosen based on a standard value of the actual concrete, which is 1.2%; the other two values are chosen considering a higher and lower order of magnitude [28]. A similar argument can be made for the activity of the water, whose measured values are shown later.

To avoid wasting unnecessary computational time, the results of the domain dimension study were used to choose a reasonable side length for a cube of water with a wall beside the detector, as

shown in Figure 6. The mentioned study was performed for a cube of only water with a detector in the center, so one could argue that the presence of the wall could badly influence the validity of the results. However, the physical meaning of the study is that after a certain distance from the detector, the gamma radiation of the radon atoms is most probably stopped before reaching the detector, so it is not interesting to simulate this part of the domain for our scope. Since the wall is made of concrete, whose density is much higher than water, keeping it inside the domain is a conservative choice because a higher density of the medium means a higher probability for the gamma radiation to be stopped, as stated by equation (8). Based on the study mentioned above, the side length of the simulated cube is 2 m, filled with water and concrete (the wall at three different distances). The geometry of the detector and its parameters are those suggested in the original g4sds program described above. Part of the code, with the simulation's FWHM parameters, is shown in Figure 12.

```
/g4sds/detector/fwhm/use true
/g4sds/detector/fwhm/f 1389
/g4sds/detector/fwhm/g 0.977
/g4sds/detector/fwhm/h 0.0
```

Figure 12. Part of the code in the "common.mac" file with the FWHM parameters.

In particular, the concrete wall is placed on the right of the domain, and it is classified inside the code as a parallelepiped-shaped sample. The detector is made of a cylindric CsI crystal with dimensions 4 cm radius and 8 cm length, and an aluminum capsule around it. To better simulate the real electronic of the detector, the code defines three parameters for the FWHM (*Full Width Half Maximum*), shown in Figure 12. As can be seen, the parameters are those for a NaI crystal, however, they are also suitable for a CsI crystal, and the values are f=1389 keV^2, g=0.977 keV, and h=0. Even if these parameters are not precise, they give a pretty good resolution value. Using equation (3), with the energy of the main radon peak (609 keV), the resolution of the detector, calculated as the ratio between the FWHM and the energy of the peak, is 7.31%, quite similar to the value of the real detectors in ArtEmis, which is ≈8% [8].

The decays are generated through a volumetric source placed in the water (for the radon) or in the wall (for the potassium). Since g4sds cannot simulate more than one radiation source, separated simulations are needed to investigate the effect of the simultaneous decay of radon and potassium, with a later sum of the two results. This is possible because the radiation from two sources and the resulting interactions can be considered independent. In order to calculate the number of events to simulate, N_e, many variables must be taken into account, and some assumptions must be made. Equation (10) has been used to do that,

$$N_e = A \cdot t = \lambda \cdot N \cdot t \tag{10}$$

where the activity A is given by the *decay constant* λ multiplied by the *atomic density* N, and the total number of events is given by the activity multiplied by the time t. However, the atomic density and the decay constant can be rewritten by introducing more variables, which are easier to use to

calculate the final value of the number of events from the concrete of the wall through the equation (11)

$$N_e = \frac{\ln(2)}{t_{1/2}} \cdot \frac{C \cdot m}{MM} \cdot N_A \cdot n \cdot t \tag{11}$$

where $t_{1/2}$ is the *half-life* of the radioisotope, C is the *mass concentration* as a percentage, m is the *total mass*, MM is the *molar mass,* N_A is the *Avogadro number*, and n is the *stoichiometric number* of the chemical formula of the molecule containing the radionuclide, namely, K_2O. For our case, the wall's mass is calculated through the density of concrete, which is around 2400 kg/m^3, and the volume can be calculated through the geometric data, different for each simulation.

In order to use geometric data also for the calculation of the number of events from the radon in water, the following equation is used:

$$N_e = A \cdot (1000\,{}^{\mathrm{l}}/_{\mathrm{m}^3}) \cdot V \cdot t \tag{12}$$

where A is the radon *activity* in the water in Bq/l, which is transformed into Bq/m^3 by multiplying by 1000 l/m^3, and V is the *volume* of the water inside the domain. This represents the total number of radon decays, however, considering the complete decay chain of the radon, simulated by Geant4 instantaneously, the mean number of gamma photons is around 4.5 per decay. To show an order of magnitude of the real activity of the water of the Italian sites, the values measured by SURO (the Czech National Radiation Protection Institute) are reported in Table 2, where the relevant information is in the last two columns [29].

Table 2. Activities of the samples from the Italian sites measured by SURO [29].

sample number	**place of collection**	**bottle**	**description of the sampling location**	**date of collection**	**measurement date**	**activity (Bq/l)**	**uncertainty (Bq/l)**
1500	Italy	1	well	20/2/23 7:25	21/02/2023	6.4	2.8
1501	Italy	2	S13 horizontal borehole	20/2/23 11:10	21/02/2023	30.8	2.9
1502	Italy	3	S15 horizontal borehole	20/2/23 11:00	21/02/2023	8.1	2.9
1503	Italy	4	S16 horizontal borehole	20/2/23 11:13	22/02/2023	3.5	1.2
1504	Italy	5	S17 horizontal borehole	20/2/23 11:17	22/02/2023	<2.9	-
1505	Italy	6	S18 horizontal borehole	20/2/23 11:02	22/02/2023	11.1	1.0
1506	Italy	7	E1 horizontal borehole	20/2/23 9:48	21/02/2023	6.0	3.0
1507	Italy	8	E3 horizontal borehole	20/2/23 10:17	21/02/2023	8.1	2.8

1508	Italy	9	E3dx horizontal borehole	20/2/23 10:19	21/02/2023	16.0	0.7
1509	Italy	10	Nodo B	20/2/23 10:16	21/02/2023	24.1	3.3
1510	Italy	11	Hall B	20/2/23 9:53	21/02/2023	<6.0	-
1511	Italy	12	Labs entrance	20/2/23 11:43	21/02/2023	1.9	0.3
1512	Italy	13	Nodo C	20/2/23 10:25	21/02/2023	8.3	0.6
1513	Italy	14	Car gallery	20/2/23 9:58	21/02/2023	<5.4	-
1514	Italy	15	water source Paganica	20/2/23 8:47	21/02/2023	<6.0	-

The mentioned measurements were performed before the installation of the ArtEmis setups in many locations in the Gran Sasso region, and they represent a reference value of the only radon activity in the water because they were made in a laboratory without the strong effects of other radiation sources such as potassium of the concrete walls. The time t considered to calculate the activity is 60 seconds. This is a low value, however, it has been chosen to keep the computing time of the simulation reasonably low. Moreover, to have values of the total number of counts that are more similar to the real case, the results of the simulations have been multiplied by a constant. The reason is that the dimensions of the real crystal in the detector are different from the simulated one (1 cm radius and 6 cm length). So, the total number of counts is multiplied by the ratio between the volume of the real crystal and the volume of the simulated one, since the events detected by the crystal are proportional to its volume.

3.4 Comparison between water and air

A comparison of simulations has been performed to better overview the consequences of having water as the medium instead of air. As already discussed, water stops particles much more efficiently due to its higher density, so the detection of the particles traveling in the medium is expected to be quite different from the case with air.

The simulation is built with a setup similar to the real site in Italy, which is composed of a cube filled with the medium, a part of the concrete wall, and a detector in the center. The side length of the cubic domain is 2 m, taking into account the study of the domain dimension previously explained, and the distance between the wall and the detector is 0.35 m. The detector is formed by a cylindric CsI crystal with a radius of 4 cm and a length of 8 cm and an aluminum capsule surrounds it. The geometry of the simulation is shown in Figure 13.

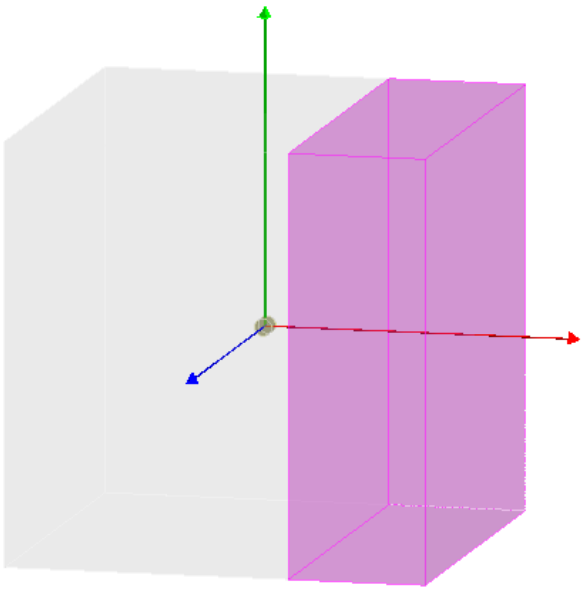

Figure 13. Geometry of the simulation of the comparison between an air and a water medium.

3.5 Comparison between real and simulated spectrum

Simulations are very useful to predict real phenomena, but they are not always precise and their results are not perfectly superimposable with the actual case. In fact, simulations usually use a simplified geometry and a simplified imitation of the real phenomenon, not considering all the possible variations of the conditions and the relevant parameters. In the frame of the studies for the ArtEmis project, it is helpful to compare the real spectrum detected in the chosen Italian site and a simulation that is as similar to the real case as possible.

Figure 14 shows the setup of site 3 in Italy, while Figure 5 already shows a scheme from which the simulation domain can be identified.

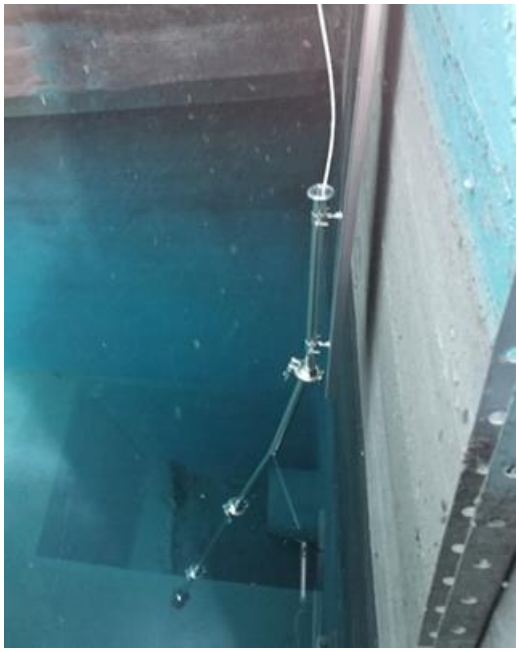

Figure 14. Picture of the real site 3 in Italy, Gran Sasso.

The side length of the cubic domain is 2 m, again taking into account the study of the domain dimensions, filled with water, and the concrete wall is at the real distance from the detector, which is calculated through the geometric data. These are the angle between the wall and the inclined bar holding the detector, 13°, and the depth from the surface of the detector, 2 m, so the distance is calculated as in equation (13)

$$d = (2\ m) \cdot \tan(13) = 0.46\ m \tag{13}$$

which is an approximate value because the slope of the bar does not begin from the surface of the water but a little above.

The detector is as similar to the real as possible, with a CsI crystal with a radius of 1 cm and a length of 6 cm, and an aluminum capsule surrounding it. However, the real detector has some additional components made of plastic and the iron bar supporting the detector which are not included in this simulation, and this could influence the final results. The parameters of the FWHM, which determine the detector's resolution, are those shown in Figure 12. The simulated events are calculated using the same equations used in section 3.3, with an activity of 20 Bq/l and a total time of 10 minutes (600 seconds). However, it is not so relevant because the final spectrum is scaled to have the same total number of detected of the real spectrum.

The data detected and transmitted from Italy are stored in several files at a frequency of one registration every two minutes, adding the new counts to the previous acquisition for every available day, and with an irregular frequency, the count is reset to start a new acquisition. However, looking at these files, not every day and not every two minutes the data acquisition is successful, and many fails are registered, even in the time range considered for this analysis, which is from the 5th of April to the 21st of May.

The spectrum from the site is not calibrated, which means that it shows the number of counts for each channel of the detector's acquisition system. The relationship between the channels and the energy is not linear, so more data are needed to perform the calibration. However, the available data, reported in Table 3, are from another site, in Greece.

Table 3. Data for the interpolation of the calibration curve.

Channels	Energy [keV]	Error [keV]
113	241	1.59
133	295	1.631
148	351	0.672
200	609	0.753
255	1120	5.68
292	1765	9.31

The interpolating curve is shown in Figure 15,

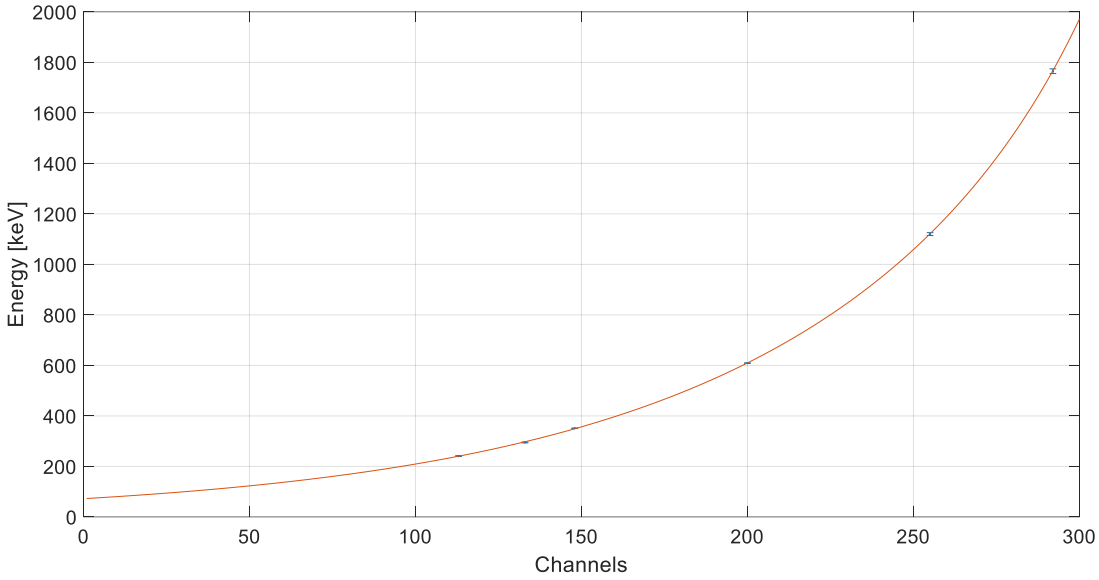

Figure 15. Calibration curve of the Greek detector.

and its equation, computed with the Matlab's curve fitter tool, is in the form

$$en = a \cdot \exp(b \cdot ch) + c \cdot \exp(d \cdot ch) \tag{14}$$

where en is the *energy*, ch is the *number of the channel*, and a, b, c, and d are the coefficients of the interpolating equation, whose values are in Table 4.

Table 4. Coefficients of the interpolating equation of the calibration curve.

	a	b	c	d
Value	72.24	0.01064	0.0006891	0.04215
Error	6.76	0.000643	0.0090451	0.0415933

However, the calibration performed is not suitable for the studied site and detector because it was performed for another site. If it is applied to the data of interest, it gives a non-physical spectrum. So this is the reason why a non-calibrated spectrum is shown in the results section.

3.6 Study of the disturbance effect of potassium

A study of the influence of ^{40}K inside the walls on the detected spectrum has been performed to understand better the statistical effect on the fluctuations of radon concentration inside water. In particular, this study aims to investigate the statistical noise of the gamma spectra in different configurations and concentrations of radon and potassium and compare it with the case of a reduced spectrum. The different parameters are the same as reported in Table 1, in section 3.3, so the variations are investigated on three activities of the water, three concentrations of potassium in the wall, and three distances between the wall and the detector.

The geometrical parameters and the materials of the simulations are the same as section 3.3 too, but the relevant results are the total number of detected counts and the error of the Poisson distribution, calculated as the square root of the first quantity. In particular, the main interest is in the ratio between the error on the total number of detected counts and the number of counts detected only from radon, because this value shows how much the effect of the variation of the radon concentration should be in order to have an evident indication in the measured data.

Moreover, there is an interest in the possibility of taking into account only a smaller range of energies instead of the full spectrum, to investigate if the disturbance effect of the potassium is lower in this case. The reduced spectrum covers an energy range from 500 to 700 keV, because it includes the most characteristic and evident peak of the radon gamma spectrum at 609 keV, so it seems the most reasonable range to analyze in order to investigate the effects of the radon concentration changes since it is likely to overcome the effects of the potassium in the wall. Instead, the full spectrum covers an energy range from 0 to 4095.5 keV, without any cut.

4 RESULTS AND DISCUSSION

In this chapter, the results obtained with the methods described in the previous chapter are compiled, analyzed, and discussed through a comparison with the existing knowledge and theory presented in the frame of reference chapter.

4.1 Energy deposited in the world

The resulting spectra for water and air are shown in Figure 16 and Figure 17.

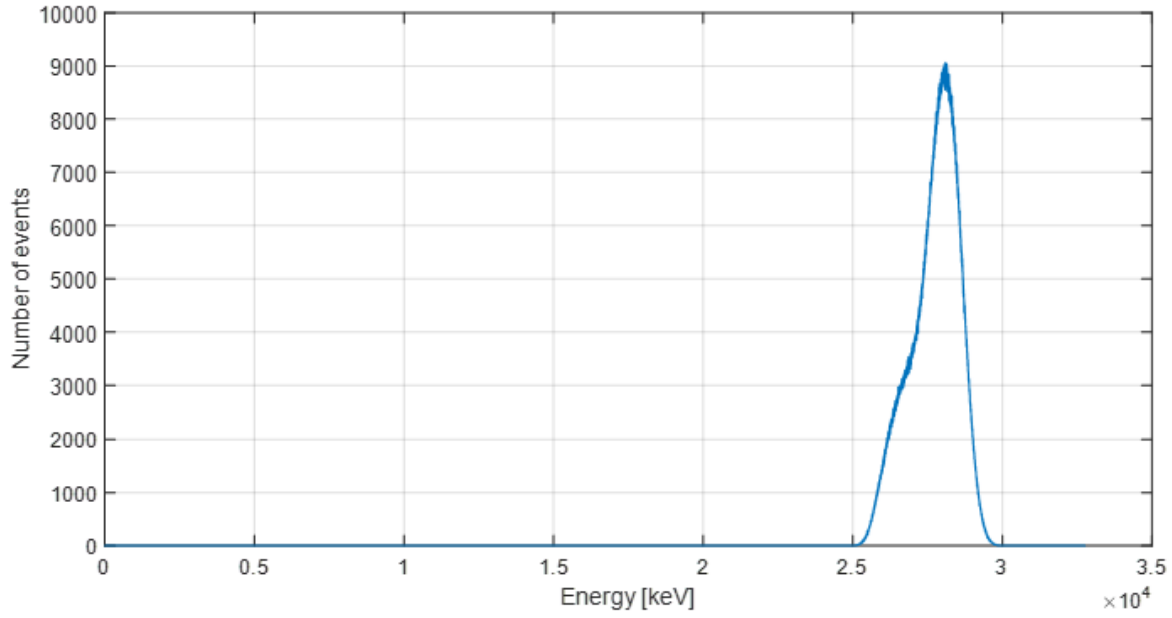

Figure 16. Gamma spectrum of the energy deposited in the simulated world made of water.

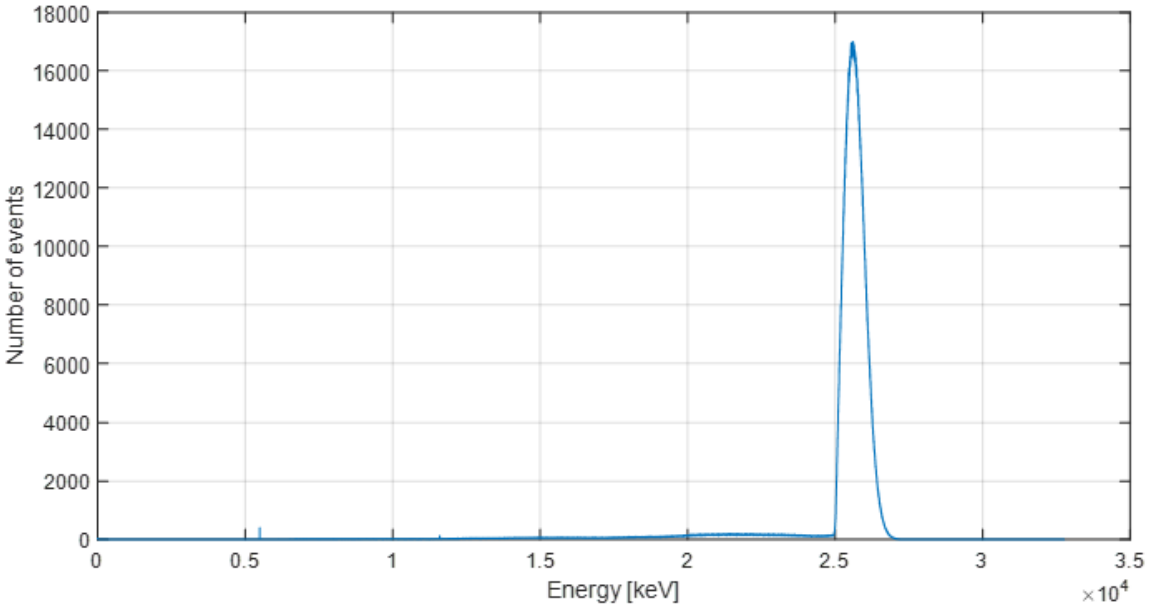

Figure 17. Gamma spectrum of the energy deposited in the simulated world made of air.

As can be seen, there are some differences between the two spectra. The two peaks have a slightly different energy, ≈28 MeV in water and ≈25.5 MeV in air. Those peaks mean that the energy deposited by all the particles produced in the decays (α, β, and γ) is summed to give the spectra. While a detector with a response time smaller than a second can detect the different events separately, with Geant4, the instantaneous decay of the whole chain is detected as a sum of the energies. However, the dominating part of the deposited energy is due to the sum of the α particles released in the decay chain (mostly from ^{222}Rn, ^{218}Po, ^{214}Po, and ^{210}Po), which is ≈25 MeV.

The peak is lower in the air because fewer particles deposit energy in the world since they are freer to travel and less likely to interact with the medium. This means that it is more probable that they escape from the simulation domain, especially beta electrons and gamma photons. Instead, in water, only particles produced in more external layers are likely to escape, so they deposit more energy in the world.

The different shapes of the two peaks are mostly due to the different quantities of beta particles interacting with the medium. In fact, according to the theory, in beta decay, two particles are produced: an electron (or a positron) and an anti-neutrino (or a neutrino). The last particle does not interact with any material, so the energy carried by them is completely lost, and the beta electrons that carry the remaining energy have a wide energy range.

4.2 Domain dimensions

The results are shown in Figures 18 and 19, which also show the standard error of the Poisson distribution.

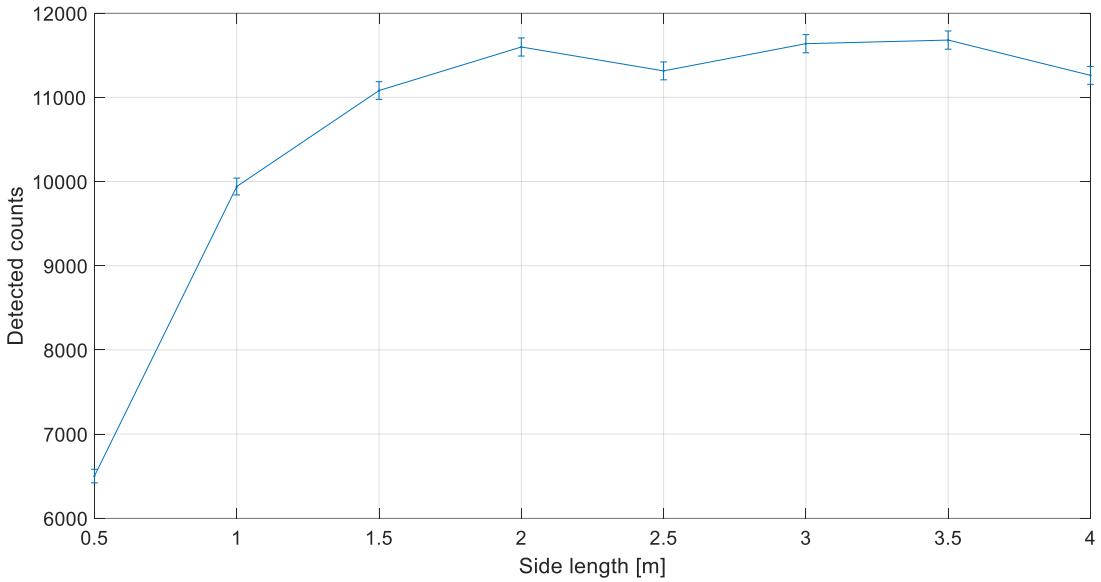

Figure 18. Plot of the number of detected counts for different side lengths of the simulated water domain.

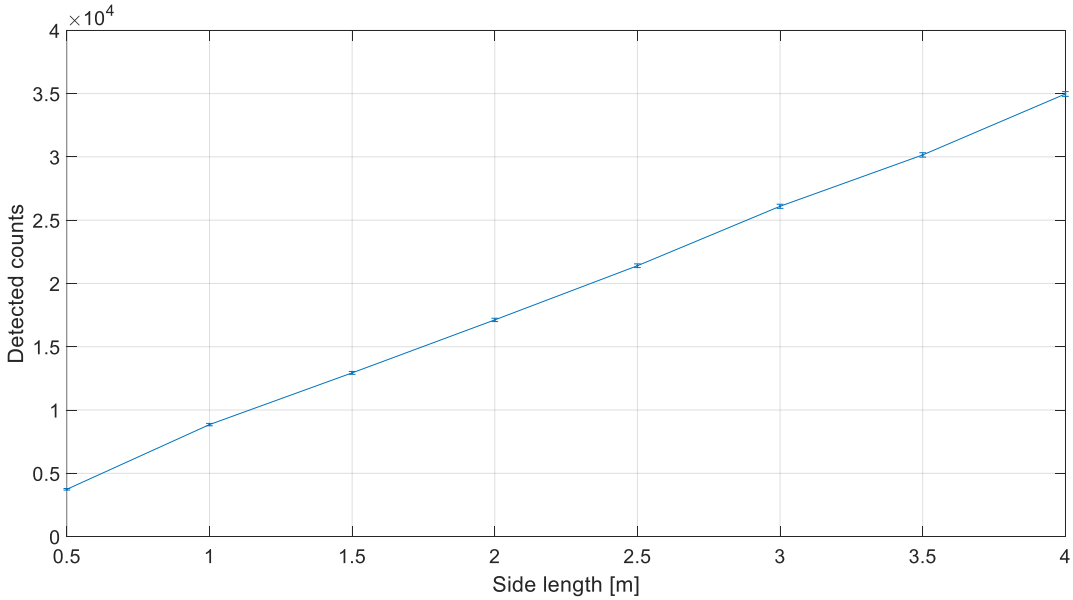

Figure 19. Plot of the number of detected counts for different side lengths of the simulated air domain.

The process reaches an almost constant value in a few simulations with the first one. In contrast, with the second one, after increasing the domain dimensions so that the computation time becomes very high, there is still a significant difference between two consecutive points.

Table 5. Points of the curve in Figure 18, with the relative difference.

Side length [m]	Detected counts	Relative difference [%]
0.5	6501	-
1	9941	34.60%
1.5	11081	10.29%
2	11599	4.46%
2.5	11315	2.51%
3	11638	2.77%
3.5	11681	0.37%
4	11262	3.72%

Table 6. Points of the curve in Figure 19, with the relative difference.

Side length [m]	Detected counts	Relative difference [%]
0.5	3737	-
1	8849	57.76%
1.5	12936	31.59%
2	17121	24.44%
2.5	21399	19.99%
3	26096	18.00%
3.5	30153	13.46%
4	34970	13.77%

As seen in Table 5, the relative difference, for the case with water, at a side length of 2 m is less than 5%. This is a good compromise between the domain dimension (because a bigger one would take a significant amount of computing time) and the relative difference (because it is sufficiently low). The result gives us information on how to choose a reasonable volume of water surrounding the ArtEmis detectors in the simulations, so, a side length of 2 m will be used for the studies in the following sections. Instead, for the case with air, in Table 6, at a side length of the domain of 4 m, the relative difference is still too high, so it would require more simulations with more significant domain dimensions to reach the desired size, with a consequent increase in the computing time.

4.3 Effects of the distance from the wall

Figures 20, 21, 22, and 23 show the effects of the wall's distance from the detector, comparing the number of counts with different concentrations and without the effect of potassium. The error bars show the Poisson errors calculated on the total number of counts (sum of counts from radon and potassium).

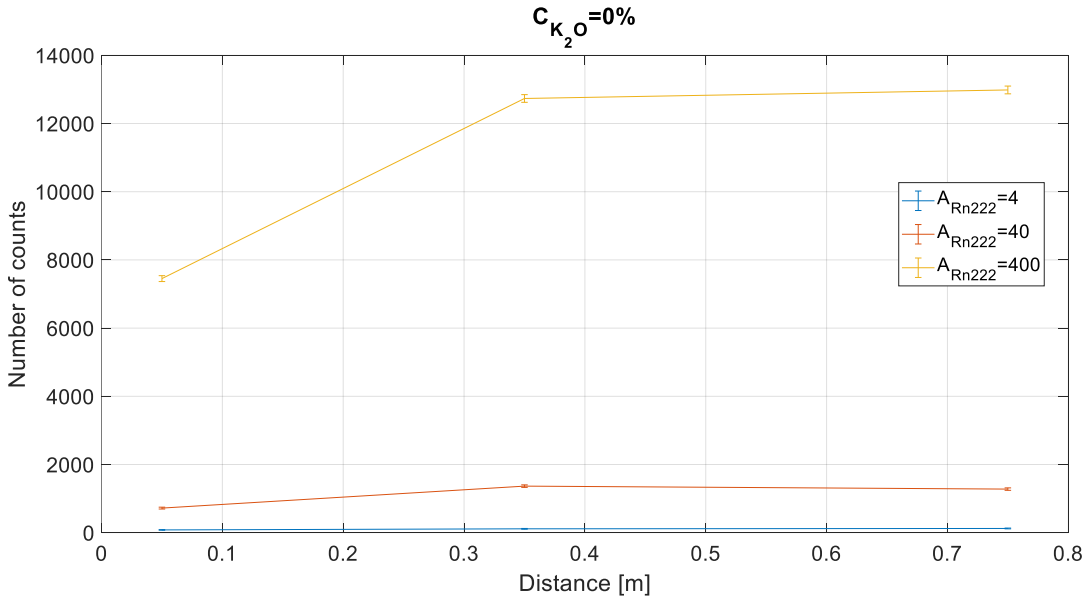

Figure 20. Plot of the total number of counts as a function of the distance for a radon activity of 4 Bq/l (in blue), 40 Bq/l (in orange), and 400 Bq/l (in yellow), with a K_2O concentration in the wall of 0%.

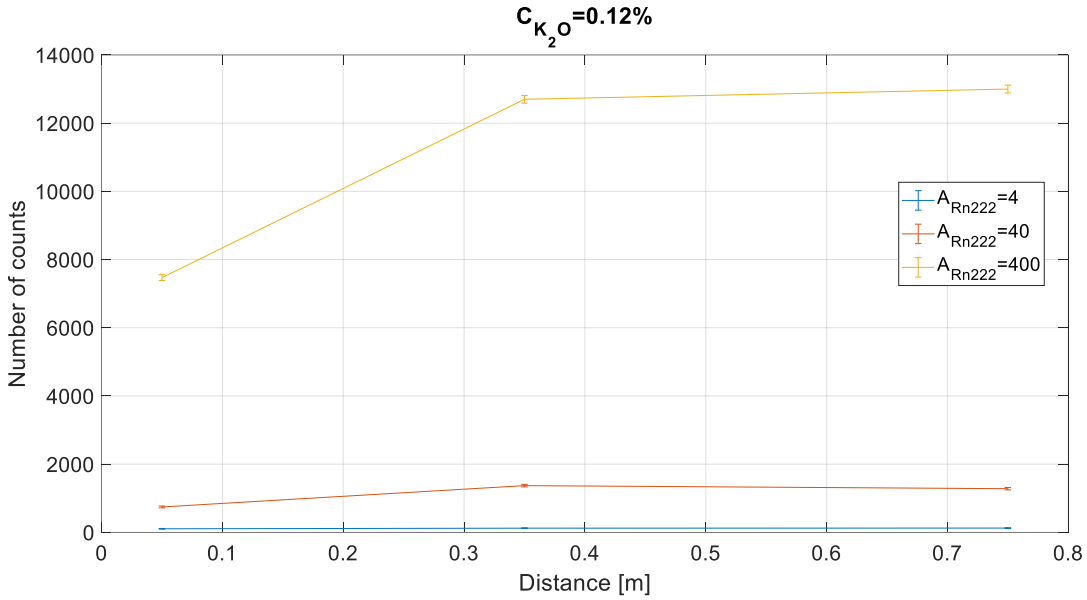

Figure 21. Plot of the total number of counts as a function of the distance for a radon activity of 4 Bq/l (in blue), 40 Bq/l (in orange), and 400 Bq/l (in yellow), with a K_2O concentration in the wall of 0.12%.

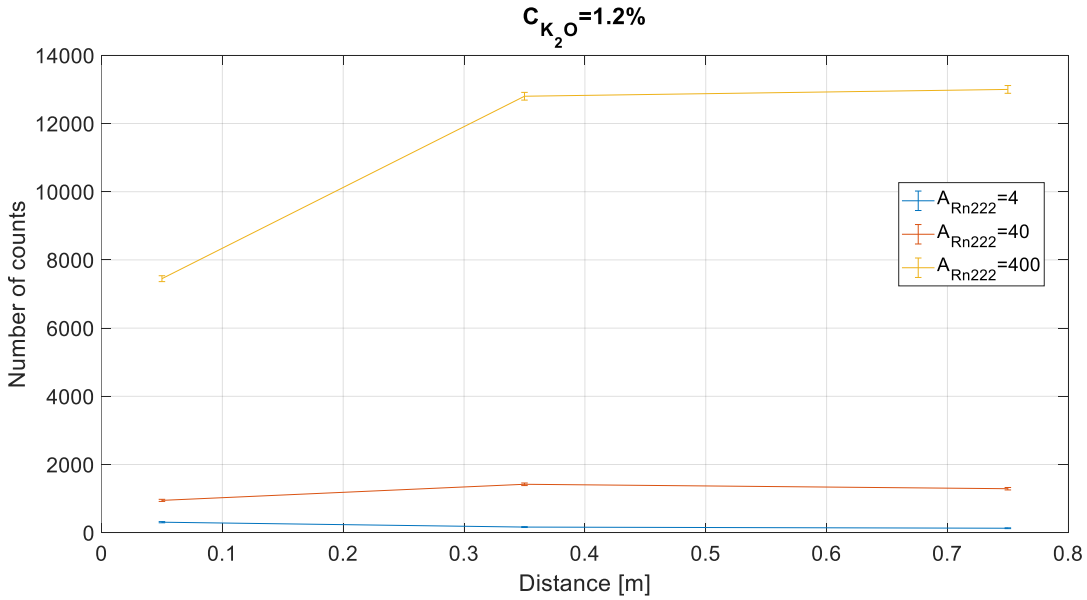

Figure 22. Plot of the total number of counts as a function of the distance for a radon activity of 4 Bq/l (in blue), 40 Bq/l (in orange), and 400 Bq/l (in yellow), with a K_2O concentration in the wall of 1.2%.

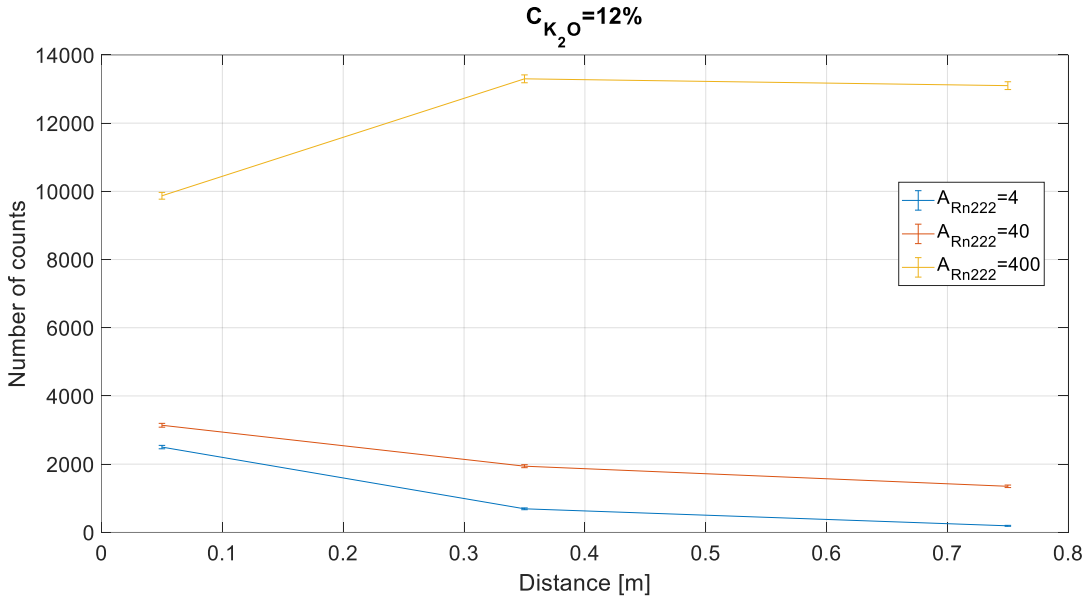

Figure 23. Plot of the total number of counts as a function of the distance for a radon activity of 4 Bq/l (in blue), 40 Bq/l (in orange), and 400 Bq/l (in yellow), with a K_2O concentration in the wall of 12%.

In the two cases with a K_2O concentration of 0.12% and 1.2%, the effect of potassium is almost irrelevant, and the plots are very similar to the case with no potassium. However, the last figure shows a significant increase in the number of counts, particularly for lower distances, which is reasonable to predict considering the higher potassium concentration in the wall. In fact, from theory, it is known that radioactivity is a physical phenomenon strongly dependent on the distance, and the effect is even more evident if the medium is water instead of air because of the higher density and the consequent higher probability of stopping the particles coming from the decays.

It is interesting to notice that, except for the case with a K_2O concentration of 12% (which is an unrealistically high value for a standard concrete), the number of detected counts seems to increase for higher distances. This can be explained by the fact that increasing the distance between the wall and the detector inside the simulation means increasing the quantity of water, which is

considered a source of radioactivity due to the radon decay. This source seems to have a more significant effect than the potassium in the wall, particularly for an activity of 400 Bq/l.

The mentioned effects can also be seen in the gamma spectra at different distances, keeping a realistic value for the radon activity (40 Bq/l) and the potassium concentration in the wall (1.2% of K_2O, because it is the most realistic value), shown in Figure 24, where a logarithmic scale is used to highlight the peaks.

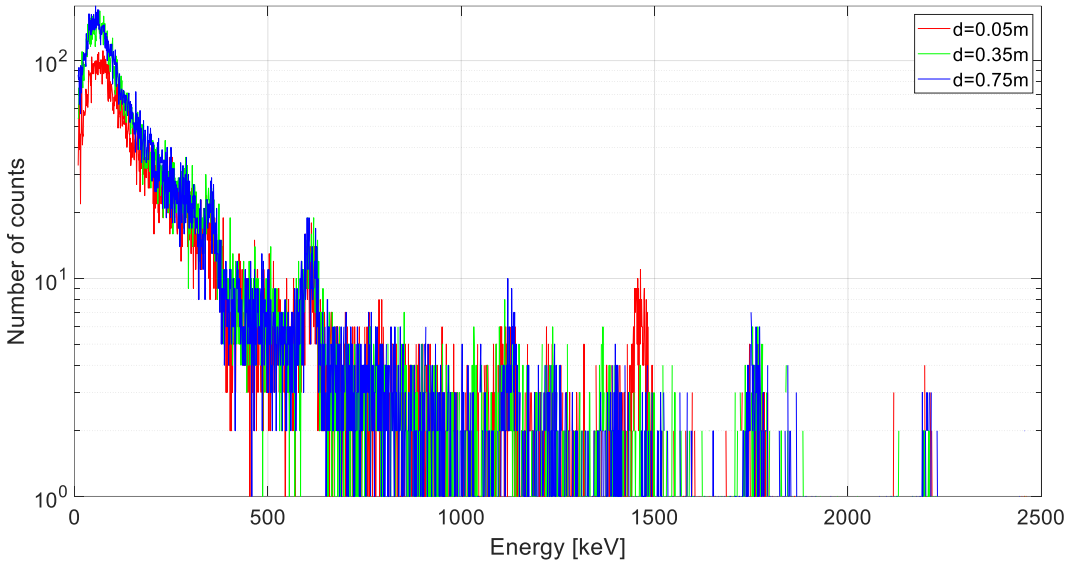

Figure 24. Comparison between the logarithmic spectra at 5 cm (in red), 35 cm (in green), and 75 cm (in blue).

In the previous figures, the energies below 10 keV are cut to eliminate the very high values, which are irrelevant to the discussion.

First of all, it is possible to see that the characteristic peak at 609 keV is evident in each spectrum, which means that the effect of potassium does not overpower it. However, the red spectrum, corresponding to a short distance from the wall, has a marked peak at 1460 keV, which is from the ^{40}K decay, and the low energy peaks from radon (351.9 and 295.2 keV), visible in the other two spectra, are almost overpowered due to the low distance from the wall. Instead, the high energy peak at 1764.5 keV from radon decay is visible in each spectrum. The increasing distance from the wall is accompanied by an increase in the low energy spectra due to the bigger amount of radon affecting them (because a more significant volume of water surrounds the detector).

In Figure 25, the spectra of the potassium present in the wall's concrete are shown without any radon effect to better understand its influence.

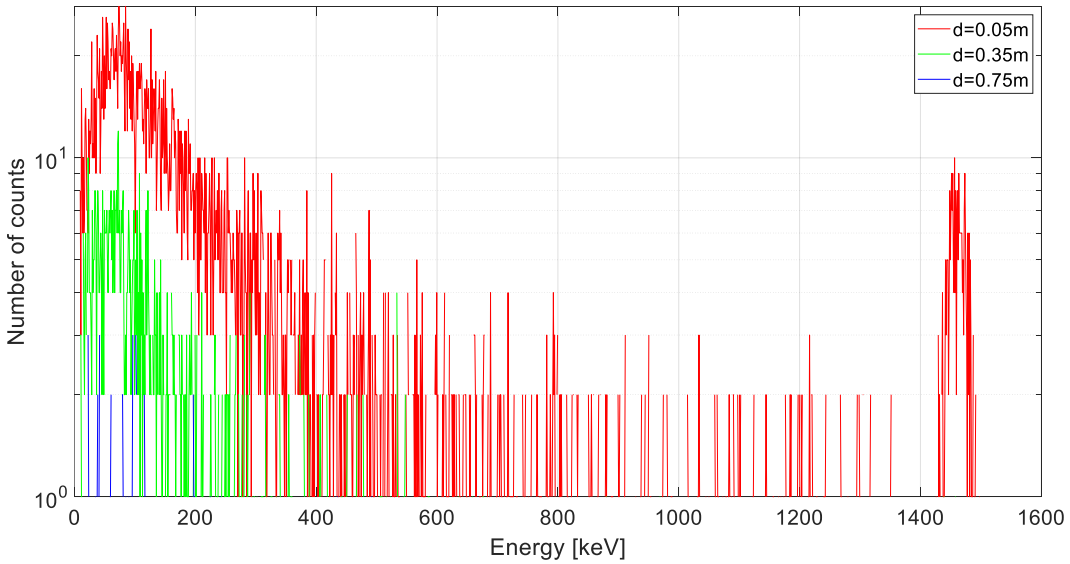

Figure 25. Comparison between the gamma spectra from the potassium in the wall at 5 cm (in red), 35 cm (in green), and 75 cm (in blue)

The only relevant effect is detected in the first case, where the detector is placed 5 cm from the wall. In this spectrum, the characteristic peak at 1460 keV is also very visible, and the Compton effect is at lower energies. In the other two spectra, counts are detected only at low energies, probably due again to the Compton scattering of the particles inside water. In fact, water is a good material for stopping radiation, so at higher distances, a very low number of counts are detected. So, in the frame of the ArtEmis project, distances from the wall lower than 5 cm are not feasible for placing the detectors, and already at 35 cm, the effects of potassium are very low.

4.4 Comparison between water and air

A clarification is needed regarding the dimensions of the considered domain. In fact, the previous results exposed in paragraph 4.2 also consider a domain filled with air. Still, it does not provide a definite dimension over which the detected counts do not change significantly because it would require a domain too big in computational costs. This means that the domain considered in this section, which has a side length of 2 m, is not enough to simulate a real case of a detector placed in an air medium. However, when comparing a gamma spectrum in water and air, this fact does not impede achieving the desired goal because it is sufficient to have the same domain dimensions for the two cases. The gamma spectra in air and water are shown in Figure 26 and Figure 27.

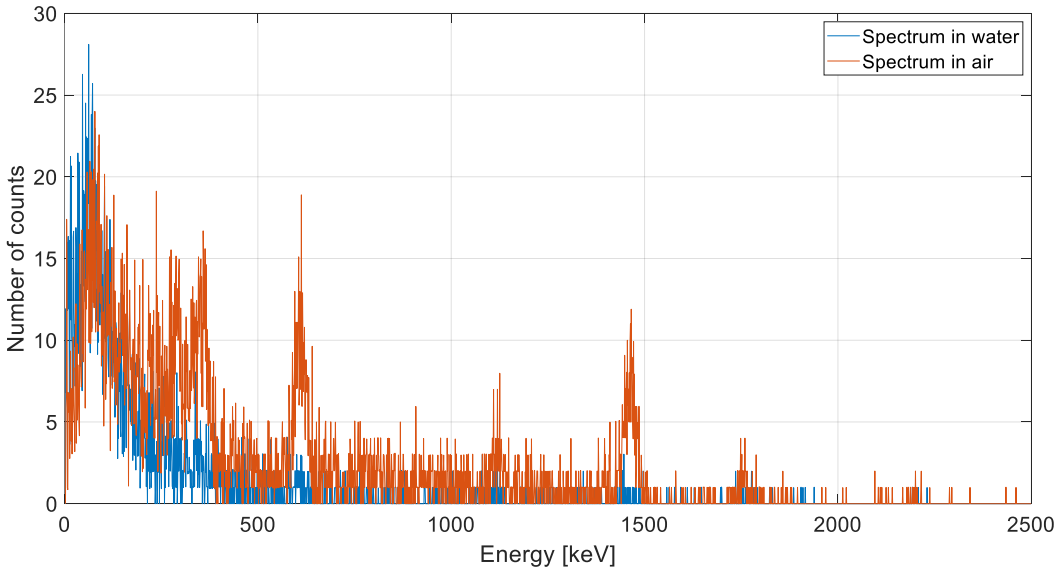

Figure 26. Simulated gamma spectrum in water (blue) and air (orange).

Even if the spectra from the simulations cover an energy range between 0.5 and 4095.5 keV, the illustrated figures cut the spectra to 2500.5 keV because higher energies do not show relevant information. A first qualitative consideration is that, as expected, peaks are more evident if the medium is air. The most visible peaks are from ^{214}Bi, which is a daughter nuclide of the radon decay chain, at 1764, 1120, and 609 keV, from ^{214}Pb, which is also part of the decay chain, at 352 and 295 keV, and from ^{40}K in the wall, at 1460 keV.

To better understand which nuclides emit the gamma photons detected in the simulated spectra, Figure 27 shows the radon decay chain with the energies of the gammas from the corresponding nuclide and one more comparison between a simulated spectrum in air and water, performed with better statistics.

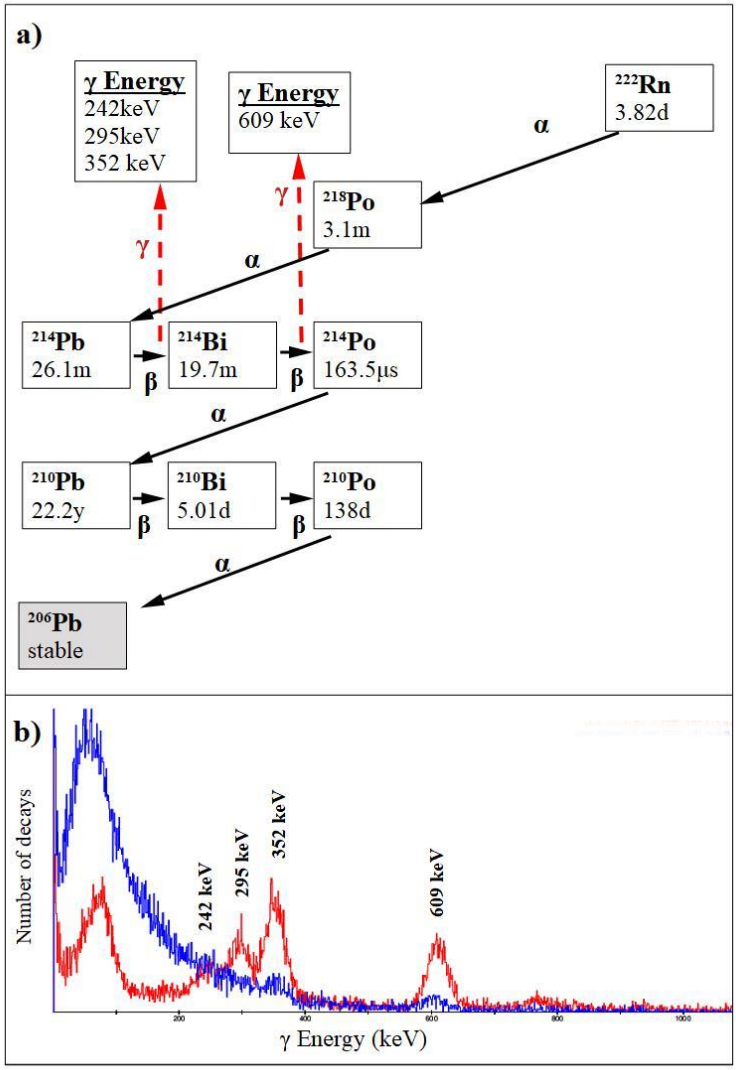

Figure 27. Radon gamma spectra in water (blue), and air (red) with the most relevant peaks highlighted [30].

The most relevant gamma energies, clearly visible in the air-simulated spectrum, are 242, 295, 352, and 609 keV, while they are less evident in the water-simulated spectrum. This can be explained again with the theory because air has a lower density, meaning that particles travel a longer distance before being scattered or stopped, particularly gamma photons, so they are more likely to reach the detector with the energy of their emission in the radioactive decay. This is also why the total number of counts detected in the case with air (6141) is much higher than in the case with water (3320). Moreover, Compton scattering is a very relevant phenomenon occurring in water, and its effect is a flattening of the spectrum, even if, in Figure 26, it is not very visible because the number of counts is relatively low. The poor statistics of the simulation results may be the reason for the differences in the spectrum shapes in the two figures. This can be seen in the shape of the peaks and the high noise of the spectra in Figure 26.

4.5 Comparison between real and simulated spectrum

In Figure 28, the real gamma spectrum without calibration is shown. The considered real site is number 3 in Gran Sasso, Italy, as mentioned in section 3.5.

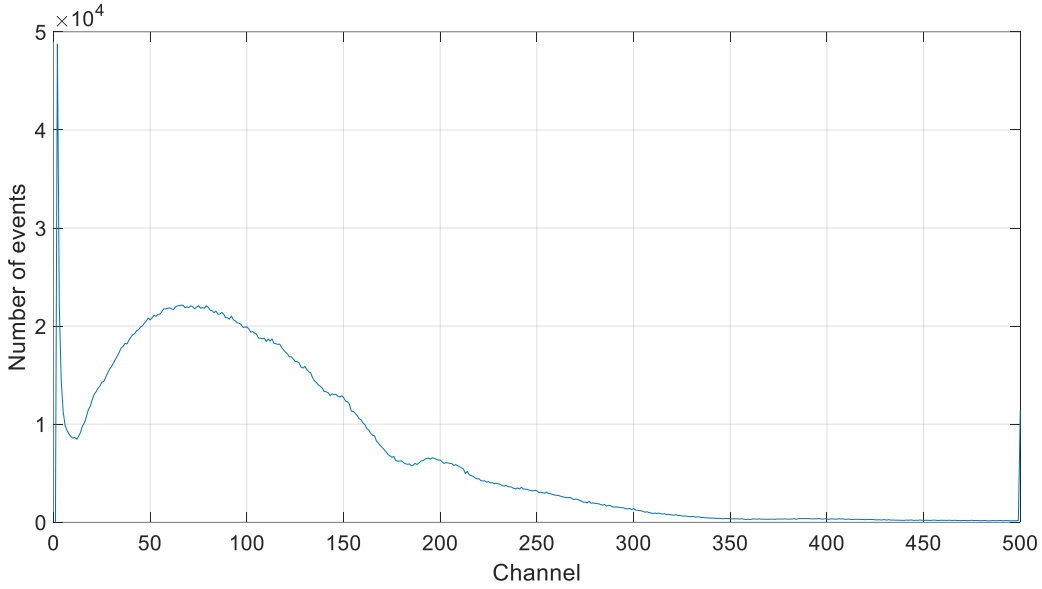

Figure 28. Real gamma spectrum from ArtEmis site 3 in Italy, in the southwest Gran Sasso tunnel, without energy calibration.

It shows the spectrum over all five hundred channels. At low energies, the noise derived mainly from the x-rays produced in the physical phenomena involved is visible. However, this noise is irrelevant to this study and creates some visual disturbance in the plot, so it will be cut in the next part of this section.

It is pretty evident the typical shape of the photopeak at 609 keV from the decay of ^{214}Bi with a strong effect of the Compton scattering at lower energies, and also a photopeak at 352 and 295 keV from the decay of ^{214}Pb. However, these peaks are not very precise because of the detectors' non-ideal functioning. The most evident inaccuracy in the spectrum is the characteristic peak at 609 keV, which seems very wide.

In Figure 29, the real spectrum is compared with the simulated one, where the last one is scaled to show, in the energy range 200-1500 keV, the same number of events of the channel range 100-400 in the other spectrum.

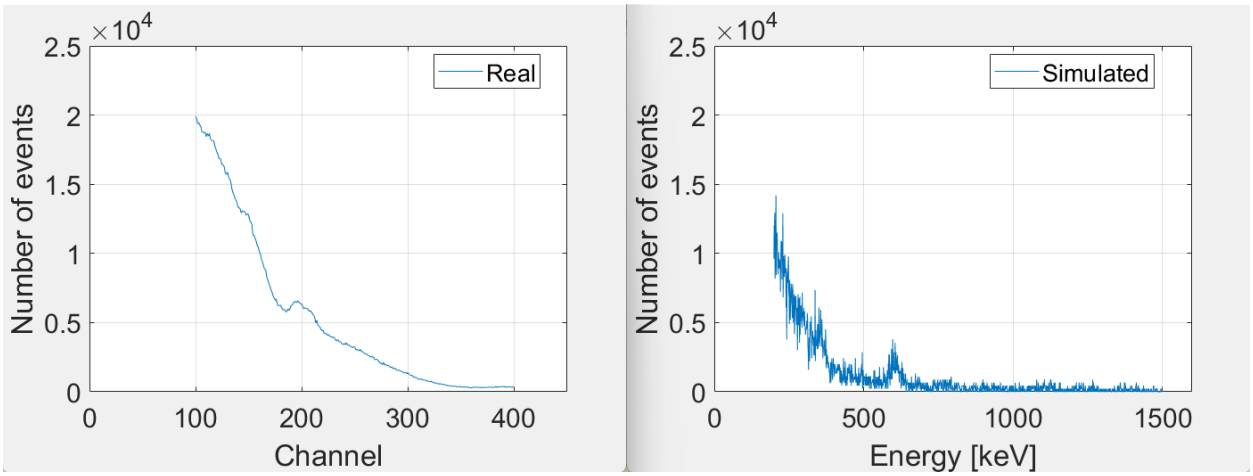

Figure 29. Comparison between the real spectrum (from ArtEmis site 3 in Gran Sasso, Italy) and the simulated one scaled to have the same number of detected counts.

The simulated spectrum has been cut at 1500 keV because higher energies do not show relevant information, and energies below 100 keV are also cut for the previously expressed reason. The peaks observed in the real spectrum can also be seen in the simulated one. Still, the two curves have some differences, such as a different slope at low energies and a lower number of counts at medium and high energies in the simulated spectrum.

In the real data, the electronic components, plastic covers, tapes, and glues used in the actual detectors (shown in Figure 30) absorb the low-energy photons and slow down many of the higher-energy ones, strongly affecting the spectrum shape.

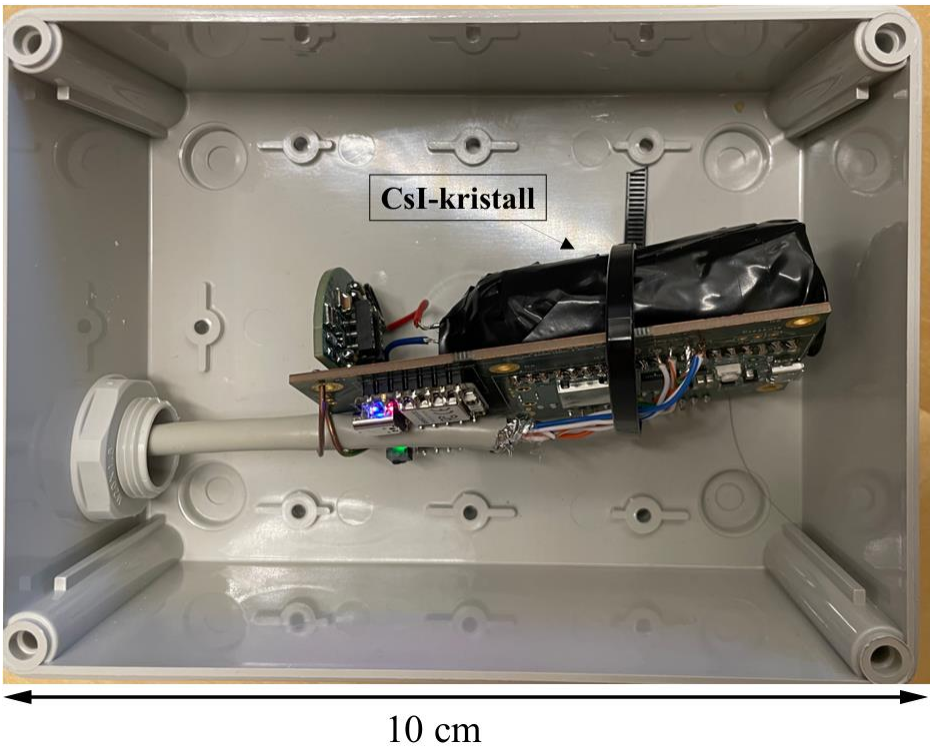

Figure 30. Picture of a sensor inside its box, with all the components exposed (made by Gururaj Kumar).

This can be seen quite well in Figure 31, which compares the low energy and low channel spectra.

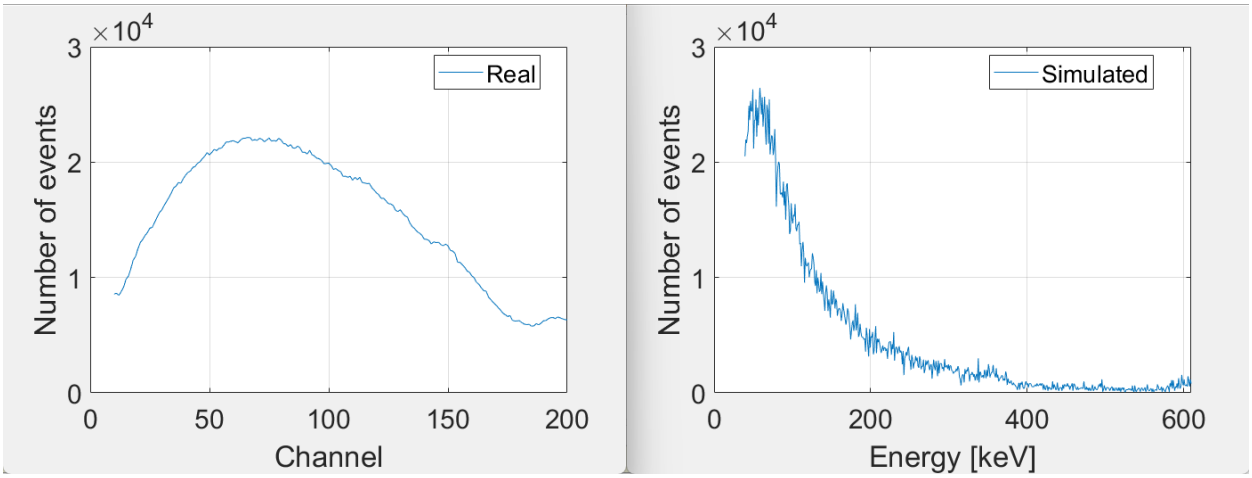

Figure 31. Comparison between the real and simulated spectra at low energy and low channels.

From the calculations of the FWHM for the simulated spectrum through equation (3), a resolution of 7.31% of the radon peak at 609.3 keV corresponds to a width of 44.54 keV. Figure 32 shows a fit of the peak which results in a FWHM of 38.63 keV, which is quite different from the theoretical value. However, a significant error is expected since the spectrum is affected by poor statistics.

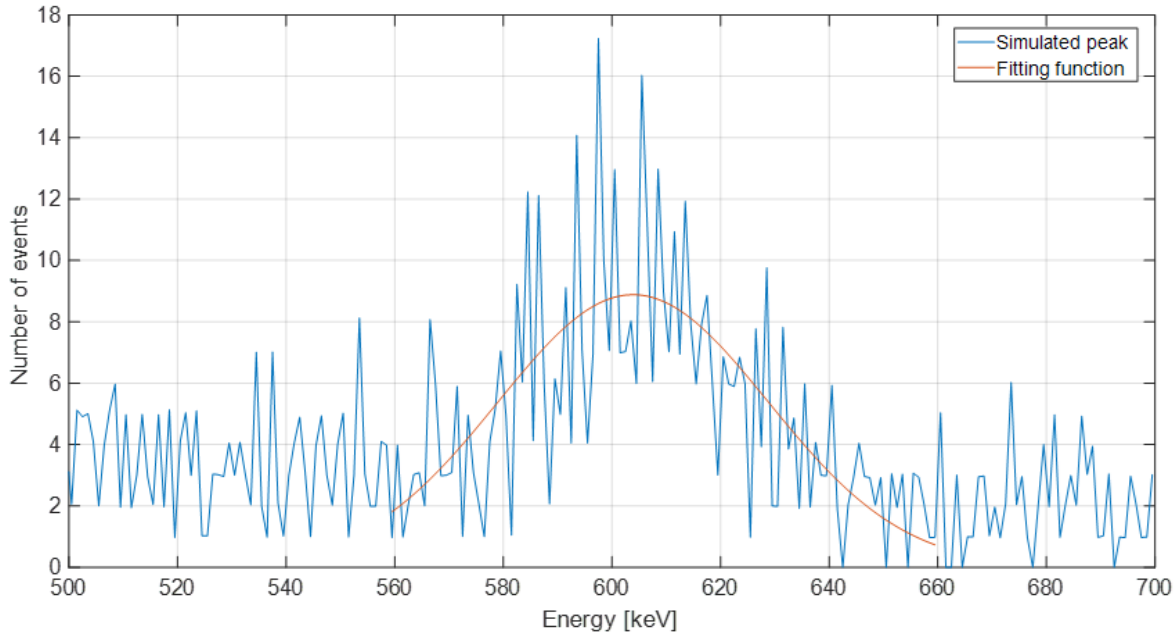

Figure 32. Fitted peak at 609 keV.

The fitting curve, performed with Matlab's curve fitter is a Gaussian whose equation is

$$y = a * e^{-\left(\frac{x-b}{c}\right)^2} \tag{15}$$

and coefficients and errors are reported in Table 7.

Table 7. Coefficients of the fitting curve of the peak

	a	b	c
Value	8.885	603.9	35.2
Error	0.989	3.3	4.95

The value of the FWHM of the fitted curve (38.63 keV) has been calculated using equation (16),

$$FWHM = 2 \cdot c \cdot \sqrt{log\left(\frac{a}{y}\right)} \tag{16}$$

which can be derived from equation (15). Moreover, the associated error can be calculated using equation (17),

$$\Delta f = \frac{\partial f}{\partial a} \cdot \Delta a + \frac{\partial f}{\partial b} \cdot \Delta b + \frac{\partial f}{\partial c} \cdot \Delta c \tag{17}$$

where f is the FWHM function, while Δa, Δb, and Δc are the errors reported in Table 7, and it gives a result of 12.95 keV. So, the FWHM of the fitted curve can be expressed in the form 38.63 ± 12.95 keV, whose range includes the value previously calculated for the simulated spectrum (44.54 keV). This is a very big error that confirms the poor statistics of the simulation.

One possible explanation for the different shapes of the real spectrum from the simulated one is that in the actual site, there are many other minor sources of radiation besides radon and potassium, which could have been underestimated in this thesis. The simulations did not include their effects because they were deemed irrelevant. Still, the non-ideal conditions of the actual case, such as anomalous concentrations, can influence the gamma spectrum. Moreover, the peaks of the real case are wider than those of the simulated one, which can be explained by the non-ideal functioning of the detector, which has many possible causes that are not always easy to understand. The Compton scattering effect at energies slightly lower than the main peak at 609 keV is more pronounced in the real case. One possible reason is the presence of obstacles which increase the probability of undergoing this type of interaction, such as the iron bar holding the detector in water.

Another possible explanation for the differences between the two spectra is that the functioning of the detectors at the Italian sites is not very convincing for many people in the ArtEmis project, so it is possible that the detected spectrum is not very reliable, in particular at lower energies, where the shape of the two spectra show more differences in the shape.

From the real data, it is also possible to calculate an approximate value of the count rate, which is the number of detected counts per second. Having the total number of counts of one acquisition and the successive, the new number of detected counts can be calculated by subtracting the two values and dividing the result by the number of seconds between the two acquisitions. These operations have been performed for the last three acquisitions of the considered data, and the resulting count rate is ≈0.75 counts per second. However, it must be pointed out that this value also includes the effect of the potassium in the wall, so the only effect of radon is slightly lower.

It is also possible to estimate an approximated order of magnitude of the activity of the water by dividing the count rate by the ratio between the volume of the detector crystal and the total volume of the water domain, by the number of liters of water, and by the average number of photons emitted per radon decay (which is 4.5), as shown in equation (18).

$$A = \frac{n}{V_{cry}/V_w \cdot l \cdot 4.5} \tag{18}$$

Again, the result was found with the approximation that the effect of the potassium in the wall and the other radiation sources is negligible. The resulting value is ≈9 Bq/l, a reasonable order of magnitude comparable with the values in Table 2.

4.6 Study of the disturbance effect of potassium

As seen in the previous sections, the effects of potassium on the gamma spectrum can be not negligible in some situations. In Figure 33, the radon spectrum is compared to the potassium effect to show the difference in the order of magnitude in one possible case (with a distance from the wall of 35 cm, a radon activity of 40 Bq/l, and a K_2O concentration in the wall of 1.2%), similar to the actual one.

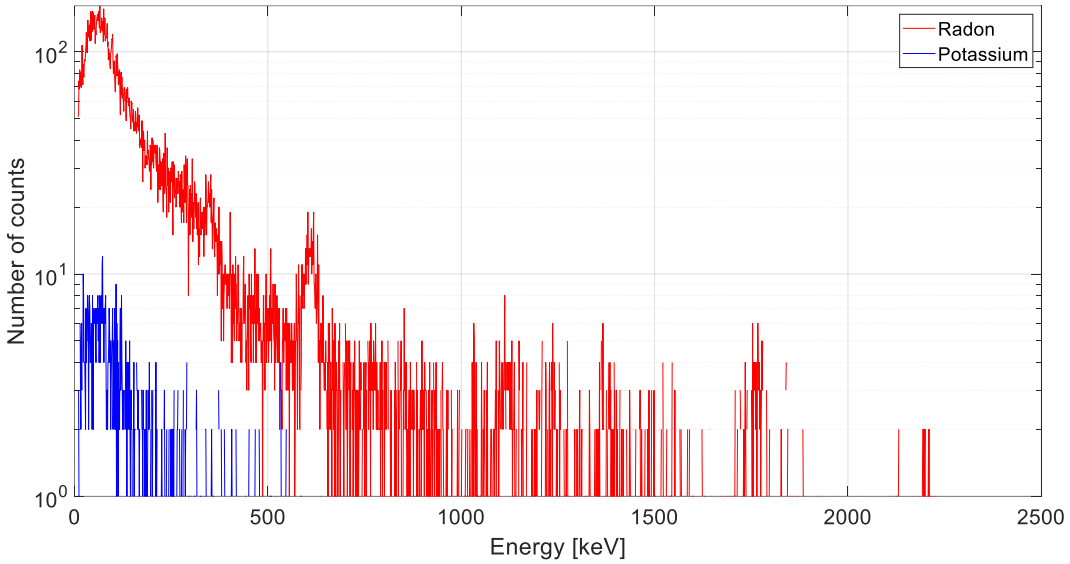

Figure 33. Comparison between the radon and potassium spectrum (d=0.35m, C_{Rn}=40Bq/l, C_{K2O}=1.2%).

In this spectrum, the counts detected from potassium are so low that the characteristic peak at 1460 keV is not present.

The results of the study described in section 3.3 are shown in Table 8 where, for every combination of potassium concentration, distance from the wall, and radon activity, it has been calculated the number of counts derived from radon, the error of the total number of counts (the sum of radon and potassium), and the ratio between the two values, all for both the full and reduced spectra. The value of the ratio is relevant in order to understand the disturbance effect of the counts derived from potassium.

Table 8. Comparison between the full spectrum error and the reduced spectrum error. C_{K2O} is the potassium concentration in the wall, d is the distance of the detector from the wall, and C_{Rn} is the radon concentration in the water.

C_{K2O}	d	C_{Rn}	Number of counts (Rn) (A)	Error (Rn+K) (B)	B/A	Number of counts (Rn) reduced (C)	Error (Rn+K) reduced (D)	D/C
0.12%	**0.05 m**	**4 Bq/l**	82	10	12,20%	4	2	50,00%
0.12%	**0.05 m**	**40 Bq/l**	722	27	3,74%	40	6	15,00%
0.12%	**0.05 m**	**400 Bq/l**	7452	86	1,15%	380	20	5,26%
0.12%	**0.35 m**	**4 Bq/l**	114	11	9,65%	6	2	33,33%
0.12%	**0.35 m**	**40 Bq/l**	1366	37	2,71%	55	7	12,73%
0.12%	**0.35 m**	**400 Bq/l**	12735	113	0,89%	549	23	4,19%
0.12%	**0.75 m**	**4 Bq/l**	124	11	8,87%	5	2	40,00%
0.12%	**0.75 m**	**40 Bq/l**	1279	36	2,81%	56	7	12,50%
0.12%	**0.75 m**	**400 Bq/l**	12985	114	0,88%	572	24	4,20%
1.2%	**0.05 m**	**4 Bq/l**	82	18	21,95%	4	4	100,00 %
1.2%	**0.05 m**	**40 Bq/l**	722	31	4,29%	40	7	17,50%
1.2%	**0.05 m**	**400 Bq/l**	7452	88	1,18%	380	20	5,26%
1.2%	**0.35 m**	**4 Bq/l**	114	13	11,40%	6	3	50,00%
1.2%	**0.35 m**	**40 Bq/l**	1366	38	2,78%	55	8	14,55%
1.2%	**0.35 m**	**400 Bq/l**	12735	113	0,89%	549	23	4,19%
1.2%	**0.75 m**	**4 Bq/l**	124	11	8,87%	5	2	40,00%
1.2%	**0.75 m**	**40 Bq/l**	1279	36	2,81%	56	8	14,29%
1.2%	**0.75 m**	**400 Bq/l**	12985	114	0,88%	572	24	4,20%

12%	**0.05 m**	**4 Bq/l**	82	50	60,98%	4	11	275,00 %
12%	**0.05 m**	**40 Bq/l**	722	56	7,76%	40	13	32,50%
12%	**0.05 m**	**400 Bq/l**	7452	99	1,33%	380	22	5,79%
12%	**0.35 m**	**4 Bq/l**	114	26	22,81%	6	5	83,33%
12%	**0.35 m**	**40 Bq/l**	1366	44	3,22%	55	9	16,36%
12%	**0.35 m**	**400 Bq/l**	12735	115	0,90%	549	24	4,37%
12%	**0.75 m**	**4 Bq/l**	124	14	11,29%	5	3	60,00%
12%	**0.75 m**	**40 Bq/l**	1279	37	2,89%	56	8	14,29%
12%	**0.75 m**	**400 Bq/l**	12985	114	0,88%	572	24	4,20%

The ratio is lower for higher numbers of detected counts because it can be approximated as $\approx \frac{1}{\sqrt{N}}$, and the counts from the potassium are much lower than those from radon.

In every case, the ratio of the error over the number of counts is lower for the full energy spectrum, which means that it is easier to measure a variation in the radon concentration in this case because the effect of the potassium in the wall is lighter. So, looking at the full spectrum seems more convenient than the reduced one.

5 CONCLUSIONS

In conclusion, this thesis investigates many topics within the ArtEmis project to produce useful results for future work. Many simulations have been performed to investigate the effects of the radon inside water and the potassium inside the wall's concrete on the detected gamma spectrum.

The study of the domain dimensions provided a result of the side length of the domain to be used for the simulations, and it has been used to choose the most suitable site for the analysis of this thesis. It has been found that the main features of the real spectrum, i.e. the main photo-peaks, are quite well reproduced in the simulated one, even if the shape is different, which means that it is possible to find valid results through computer simulations. The disturbance effects of the potassium inside the wall of the studied site strongly depend on the distance to the detector. So, since the water is an excellent screen for the radiation produced in the decays, the disturbance effect is negligible at a reasonable distance. Finally, it has been studied the possibility of considering a smaller energy range of the spectrum around the radon characteristic photo-peak instead of the full spectrum, and the results showed that the disturbance effect of the potassium is more relevant in that case, so it is not convenient to look at it.

Many of these results will be helpful for the future development of the ArtEmis project because they focus on some of the main issues that came up during the discussions with the professors and the students working on the project. The ultimate goal is to understand the behavior of the radon inside the water near the occurrence of an earthquake, to evaluate the possible development of a strategy to predict it well in advance, and the hope is that this thesis will be a further step toward this goal.

6 FUTURE WORK

One possible evolution of the sites' setup is to adopt alpha detectors instead of the currently used scintillators, which only detect gamma photons. The idea is to create a plastic membrane around the detector that is only permeable to the radon inside the water because alpha particles produced in the radon decays travel a meager distance before being stopped. This should give a clearer picture of the radon effects. However, there are some challenges to overcome, e.g., the disturbance of the radon already present in the air surrounding the detector because it could influence or even hide the effects of the radon from the water. More generally, there is still much work to be done to improve the setups of the sites and the understanding of the results. Many sites still need the installation of a detector to start the data acquisition and some of those already installed show anomalies in their functioning.

Regarding the work of this thesis, there are many possible continuations and implementations for the future. Every topic of this work can be further explored, more parameters can be changed, and all the ranges can be increased to extend the validity of the results. The same work done with the chosen Italian site can be developed with other sites, such as the Swiss site of Brunello, where an unexpectedly high radon activity has been measured. As discussed in section 3.5, the available data for the calibration are from a Greek site, so they are unsuitable for the used detector. To improve the results of this thesis, an improved calibration is required, possibly based on data obtained from the sensor under consideration, because this would allow us to compare the simulated spectrum with the real one directly. Moreover, the simulated detector can be better described with further information and knowledge of the coding in Geant4.

7 REFERENCES

[1] “Artemis – A new site tagged WordPress”, *Artemisproject.eu*, 2022. https://artemisproject.eu (accessed Aug. 12, 2024).

[2] G. Igarashi et al., “Ground-Water Radon Anomaly Before the Kobe Earthquake in Japan”, Science, vol. 269, no. 5220, pp. 60–61, Jul. 1995, doi: https://doi.org/10.1126/science.269.5220.60.

[3] I. P. Dobrovolsky, S. I. Zubkov, and V. I. Miachkin, “Estimation of the size of earthquake preparation zones”, Pure and Applied Geophysics PAGEOPH, vol. 117, no. 5, pp. 1025–1044, 1979, doi: https://doi.org/10.1007/bf00876083.

[4] J. Planinic, V. Radolic, B. Vukovic Nuclear Instruments and Methods in Physics Research A 530 (2004) 568–574

[5] “Introduction to Geant4 Release 11.2 Geant4 Collaboration”, 2023. Available: https://geant4-userdoc.web.cern.ch/UsersGuides/IntroductionToGeant4/fo/IntroductionToGeant4.pdf.

[6] T. Bäck, *Radiation protection, Dosimetry, and Detectors*, KTH, Stockholm, 2023.

[7] “Silicon Photomultiplier (SiPM) Amplified Detectors”, Thorlabs.com, 2024. https://www.thorlabs.com/newgrouppage9.cfm?objectgroup_id=15959 (accessed Oct. 10, 2024).

[8] Private communication with Gururaj Kumar.

[9] P. Törngren, “Inferring Changes in Groundwater Radionuclide Concentration: A Step Toward Earthquake Forecasting Using Measurements of Groundwater Radioactivity”, Dissertation, 2024.

[10] M. Walfridson, “Using Geant4 to simulate ArtEmis-like setups”, Dissertation, 2024.

[11] T.B. Yanovskaya, 2008, “Basics of Seismology” (St. Petersburg: St. Petersburg University).

[12] P.M. Shearer, 2009, “Introduction to Seismology” (Cambridge: Cambridge University Press).

[13] Sergey Pulinets and Dimitar Ouzounov, “What is the meaning of a short-term earthquake forecast?”, *IOP Publishing eBooks*, pp. 1–16, Dec. 2018, doi: https://doi.org/10.1088/978-0-7503-1248-6ch1.

[14] Gelfand I M, Guberman S A, Izvekova M L, Keilis-Borok V I and Ranzman E Ja 1972 Criteria of high seismicity determined by pattern recognition Dev. Geotecton. 13 415–22.

[15] Keilis-Borok V I 1990 Intermediate-term earthquakes prediction: models, algorithms, worldwide tests Phys. Earth Planet. Inter. 61 1–139.

[16] Martinelli G 1998 Earthquakes, prediction. Sciences of the Earth, an encyclopedia of events People, and Phenomena ed G A Good (London: Garland Publishing) p 192–6.

[17] “European Atlas of Natural Radiation”, *remon.jrc.ec.europa.eu*. https://remon.jrc.ec.europa.eu/About/Atlas-of-Natural-Radiation.

[18] N. Azillah and S. Fatahiyah, “A Review of Uranium Extraction from Seawater: Recent International R & D”. Available: https://inis.iaea.org/collection/NCLCollectionStore/_Public/44/100/44100529.pdf.

[19] N. K. Ryzhakova, “A new method for estimating the coefficients of diffusion and emanation of radon in the soil”, *Journal of Environmental Radioactivity*, vol. 135, pp. 63–66, Sep. 2014, doi: https://doi.org/10.1016/j.jenvrad.2014.04.002.

[20] M. Neznal, M. Neznal, and J. Šmarda, “Assessment of radon potential of soils—a five-year experience”, Environment International, 1996. doi:10.1016/s0160-4120(96)00189-4

[21] A. Lindmark and B. Rosen, “Radon in soil gas — Exhalation tests and in situ measurements”, Science of The Total Environment, 1985, doi: https://doi.org/10.1016/0048-9697(85)90243-8.

[22] E. M. Kovach, “Meteorological influences upon the radon-content of soil-gas”, Transactions, American Geophysical Union, 1945, doi: https://doi.org/10.1029/tr026i002p00241.

[23] H. W. Kraner, G. L. Schroeder, and R. D. Evans, "Measurements of the Effects of Atmospheric Variables on Radon-222 Flux and Soil-Gas Concentrations. The Natural Radiation Environment", Chicago: University of Chicago Press, 1964.

[24] W. E. Clements and M. H. Wilkening, “Atmospheric pressure effects on222Rn transport across the Earth-air interface”, Journal of Geophysical Research, 1974, doi: https://doi.org/10.1029/jc079i033p05025.

[25] H. Arvela, O. Holmgren, and P. Hänninen, “EFFECT OF SOIL MOISTURE ON SEASONAL VARIATION IN INDOOR RADON CONCENTRATION: MODELLING AND MEASUREMENTS IN 326 FINNISH HOUSES”, Radiation Protection Dosimetry, 2015, doi: https://doi.org/10.1093/rpd/ncv182.

[26] W. R. Leo, *Techniques for Nuclear and Particle Physics Experiments*. Springer Science & Business Media, 2012.

[27] “NIST: X-Ray Mass Attenuation Coefficients - Table 4”, *Nist.gov*, 2020. https://physics.nist.gov/PhysRefData/XrayMassCoef/tab4.html.

[28] “Concrete and air pollutants – Nils Malmgren AB”, *Nilsmalmgren.com*, 2024. https://www.nilsmalmgren.com/epoxy-chemistry/concrete-and-air-pollutants/ (accessed Aug. 10, 2024).

[29] “Home | SURO”, *Suro.cz*, 2024. https://www.suro.cz/en (accessed Nov. 02, 2024).

[30] Ayse Atac Nyberg and Ramon Wyss, Kosmos Year Book of the Swedish Physical Society, 2024, Jubileum edition nr 100.